SMAP Twice-Daily
SAR and SIR-Enhanced Scatterometer
EASE-Grid 2.0 Radar Backscatter

Algorithm Theoretical Basis Document
Version 1.0
January 2, 2023

David G. Long[1], Julie Z. Miller[2]

[1] *Microwave Earth Remote Sensing Laboratory, Brigham Young University, Provo, UT, USA*

[2] *Earth Science and Observation Center, Cooperative Institute for Research in Environmental Sciences, University of Colorado, Boulder, CO, USA*

Contents

List of Figures

List of Tables

1 Revision History

Table 1: *ATBD Revision History*

Revision	Date	Purpose
1.0	2022-09-13	Initial Revision

Table 2: *Data Set Revision History*

Revision	Date	Purpose
1.0	2022-09-01	Initial Revision

2 Acronyms and Abbreviations

Table 3: *List of Acronyms and Abbreviations*

AMSR-E	Advanced Microwave Scanning Radiometer-Earth Observing System
ATBD	Algorithm Theoretical Basis Document
AVE	Weighted averaging algorithm image formation algorithm
BYU	Brigham Young University
CDR	Climate Data Record
CETB	Calibrated Passive Microwave Daily EASE-Grid 2.0 Brightness Temperature
CF	Climate and Forecast Metadata Conventions
DAAC	Distributed Active Archive Center
dB	decibel $(10\log_{10})$
DIB	Drop-in-the-bucket averaging (used to produce GRD products)
EASE-Grid	Equal-Area Scalable Earth Grid (Original Definition)
EASE-Grid 2.0	Equal-Area Scalable Earth Grid Version 2.0
EASE2-M	EASE-Grid 2.0, Mid- and Low-Latitude Cylindrical Projection
EASE2-N	EASE-Grid 2.0, Northern Hemisphere Projection
EASE2-S	EASE-Grid 2.0, Southern Hemisphere Projection
EASE2-T	EASE-Grid 2.0, Temperate and Tropical Cylindrical Projection
EIA	Earth Incidence Angle
EOSDIS	Earth Observing System Data and Information System
ESDR	Earth System Data Record
FCDR	Fundamental Climate Data Record
GHz	GigaHertz
GRD	(Drop-in-the-bucket) Gridding Method
ltod	Local-time-of-day
MEaSUREs	Making Earth System Data Records for Use in Research Environments
MHz	MegaHertz
MRF	Measurement Response Function
NASA	National Aeronautics and Space Administration
NOAA	National Oceanic and Atmospheric Administration
NORAD	North American Aerospace Defense Command
NSIDC	National Snow and Ice Data Center
NetCDF	Network Common Data Format
PRF	Pulse repetition frequency
PSRF	Pixel spatial response function
rSIR	Radiometer version of SIR
SAR	Synthetic Aperture Radar

SCP	Scatterometer Climate Record Pathfinder
SIR	Scatterometer Image Reconstruction
SDR	Sensor Data Record
Sigma-0	Normalized radar cross section or backscatter (σ^o)
SIR	Scatterometer Image Reconstruction
SMAP	Soil Moisture Active Passive
TBD	To be determined
TLE	Two-Line Element
UTC	Coordinated Universal Time

3 Purpose of this Document

The Soil Moisture Active-Passive (SMAP) Mission was designed to produce globally-derived soil-moisture maps every 2-3 days. The original SMAP mission concept relied on synergistic measurements from both radar and radiometer instruments, with radar measurements produced at higher spatial resolutions than radiometer measurements. Data products were planned to use both radar and radiometer measurements to provide higher resolution products (Entekhabi et al., 2010, Entekhabi et al., 2014). Unfortunately, the loss of the radar instrument on July 7, 2015, only 83 days after launch, compromised the ability to meet spatial resolution mission requirements for soil moisture and freeze-thaw products.

The SMAP radar was the first satellite instrument to provide global L-band radar observations of global normalized radar cross section (σ^o) at multiple resolutions. The SMAP radar collected high resolution ($\sim$1-3 km) synthetic aperture radar (SAR) measurements over most of the Earth's land mass. It simultaneously collected low resolution full-footprint 29$\times$36 km measurements and higher resolution 5$\times$30 km "slice" measurements.

The SMAP radar was designed to make vegetation roughness measurements in support of the SMAP primary mission to measure soil moisture, but the radar data is useful for a variety of applications, particularly in the polar regions. Unfortunately, limitations in the data download volume precluded downlink of high resolution data over Antarctica, sea ice in the polar regions, and various islands. Nonetheless, low resolution slice and footprint data were collected and downlinked over these areas. To exploit this data, we employ image reconstruction techniques to create twice-daily enhanced resolution SMAP radar images from the slice and footprint measurements, along with twice-daily SAR images. The new data set is provided to the science community to support cryosphere and climate studies.

4 SAR and SIR-Enhanced SMAP Product Description

4.1 Product Description

The SAR and SIR-Enhanced SMAP radar (*SAR-SIR-SMAP*) data product (Miller et al., 2022) includes Level 1 gridded, twice-daily, radar backscatter data for the three SMAP 1.27 GHz radar channels (horizontal-horizontal [HH], vertical-vertical [VV] and cross polarization [X-pol: HV and VH, or X]). Data are gridded to the EASE-Grid 2.0 Azimuthal and Cylindrical projections (Brodzik et al., 2012, 2014), at various spatial resolutions, as described below. The gridded *SAR-SIR-SMAP* product is archived and distributed by the NASA National Snow and Ice Data Center (NSIDC) Distributed Active Archive Center (DACC) (`https://nsidc.org/data/NSIDC-0774/versions/1`). EASE Grids Ancillary Grid Information, Version 1 (`https://nsidc.org/data/nsidc-0772/versions/1`) provides arrays of the latitude and longitude at the center of each grid cell.

Input data for the *SAR-SIR-SMAP* v1.0 product, released in spring 2022, are the SMAP L1B Radar Half-Orbit Sigma0, Version 1 (SPL1BS0) and the SMAP L1B Radar Half-Orbit Sigma0, Version 1 (SPL1CS0) (West, 2014). Using the quality flag on the input data, only the highest quality measurements are included in *SAR-SIR-SMAP* product. The data coverage is global for days 103 through 186 of 2015.

4.2 SMAP Instrument

The SMAP instrument is based on a 6 m conically-scanning reflector antenna with a common L-band feed shared by the radar ($1.26\,\mathrm{GHz}$) and radiometer ($1.4135\,\mathrm{GHz}$). The reflector rotates about the nadir axis, producing the conically scanning antenna beam with a one-way 3 dB effective field of view measuring $39{\times}47$ km at an Earth incidence angle of $40°$ at the beam center. The swath width is approximately 1000 km wide, see Fig. 6. The two-way footprint size is $18{\times}30$ km. The rotating antenna beam enables the sensor to look in both the fore and aft directions (Piepmeier et al., 2017, West, 2014). Originally, SMAP products were produced using both radiometer and radar measurements (Entekhabi et al., 2010). After the failure of the SMAP radar instrument on July 7, 2015, the SMAP radiometer continued to function (Piepmeier et al., 2017).

The SMAP radar produced σ^o measurements at several resolutions. The highest resolution, available over only selected areas, is processed using an unfocused SAR algorithm. This is the SL1CS0 source. Global radar data was collected in a scatterometer mode at footprint and 'slice' resolutions in SL1BS0. As described below, twice-daily global images were created by gridding SAR data. The SIR algorithm is applied to the footprint and slice resolution data and provided enhanced spatial resolution σ^o by exploiting the irregular patterns of measurement locations and signal oversampling (from overlaps in adjacent footprints and overlapping swaths).
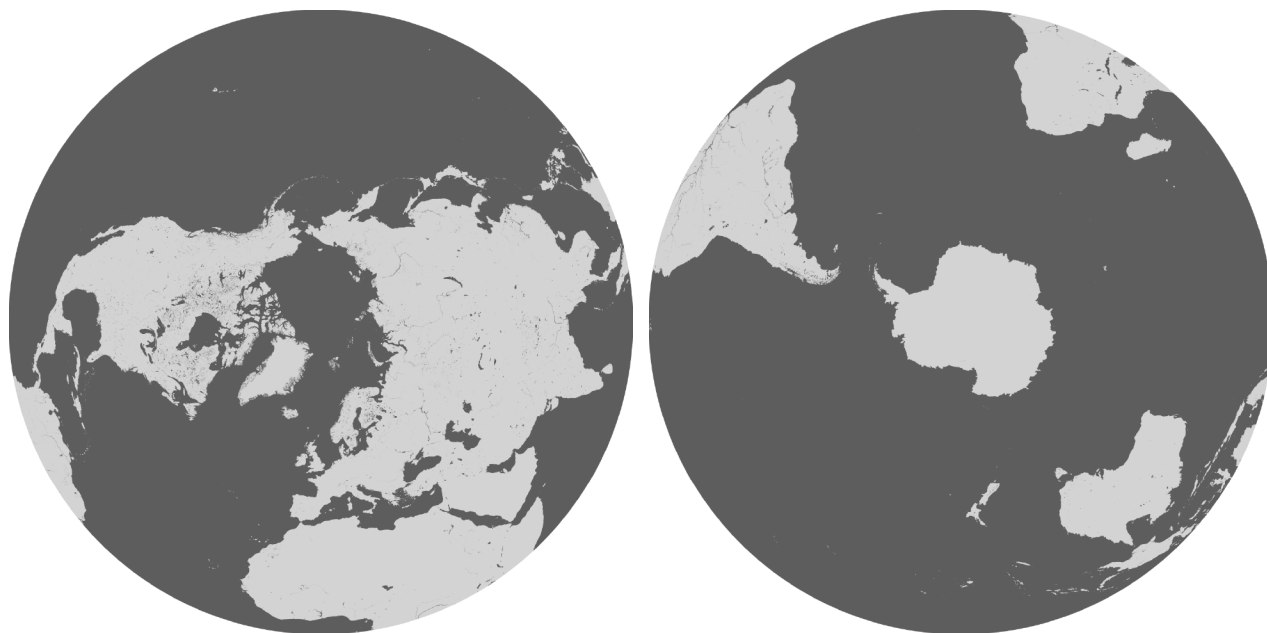
Figure 1: *Northern and Southern EASE-Grid 2.0 projection extents. Land-ocean mask from Brodzik and Knowles (2011).*

4.3   Grid Spatial Extent

Azimuthal *SAR-SIR-SMAP* grids extend to the full Northern (EASE2-N) and Southern (EASE2-S) hemispheres, respectively, as described in Brodzik et al. (2012, 2014) (Fig. 1). The spatial extent of the equal-area cylindrical projections (Fig. 2 and Fig. 3) is defined to match the extent of the Mid-Latitude (EASE2-M) grid, extending to $\pm85.044\,566\,4°$ latitude, that has been adopted by the SMAP user community. The Temperate and Tropical (EASE2-T) grid, limited to latitudes equatorward of $\pm67.1°$, is consistent with the original CETB products defined for similar scanning radiometers (Brodzik et al., 2021). See Appendix A Table 9 for grid specifications.

4.4   Grid Spatial Resolution

SAR-SIR-SMAP grid resolutions are defined relative to a SI25km base resolution: $25\,\mathrm{km}$ grids and $3.125\,\mathrm{km}$, which include EASE2-N, EASE2-S and EASE2-T grids that are compatible with the MEaSUREs CETB data products (Brodzik et al., 2021). Nested resolutions relative to the CETB $25\,\mathrm{km}$ base grids are defined using exact divisors of 2, as illustrated in Figure 4. *SAR-SIR-SMAP* projection extents, dimensions and grid cell size details are included in Appendix A. Grids used for *SAR-SIR-SMAP* processing are included in Table 4.

Figure 2: *Cylindrical EASE-Grid 2.0 projection extents. Full extent coverage is EASE2-M, with horizontal red lines delineating the smaller latitudinal extent of EASE2-T grid. Land-ocean mask from Brodzik and Knowles (2011).*

Table 4: SAR-SIR-SMAP *EASE-Grid 2.0 base grids produced, by projection and reconstruction algorithm. See Section 5 for GRD and rSIR reconstruction details.*

EASE2-M	EASE2-N	EASE2-S	EASE2-T
n/a	25km (GRD)	25km (GRD)	25km (GRD)
n/a	3.125km (GRD/SIR)	3.125km (GRD/SIR)	3.125km (GRD/SIR)

4.5   Data Products

The *SAR-SIR-SMAP* radar image products at the NSIDC DAAC covers the period beginning 31 Mar 2015 to 5 Jul 2015 (doy 103 to 186). During the initial 8 days, default SAR data selection tables were used. These provided small, even-spaced patches of SAR data. Later the control tables were updated to collect data over most land regions. Images were made with all available radar data not flagged as "bad". No calibration corrections were applied to the data. Table 5 summarizes available *SAR-SIR-SMAP* radar image products, which are all in CETB-standard EASE-2 Grid projections. The "Corrections" referred to in Tab. 5 refer to the computation of the azimuth and incidence angle model. The reported σ^0 value removes the azimuth and incidence angle effects.
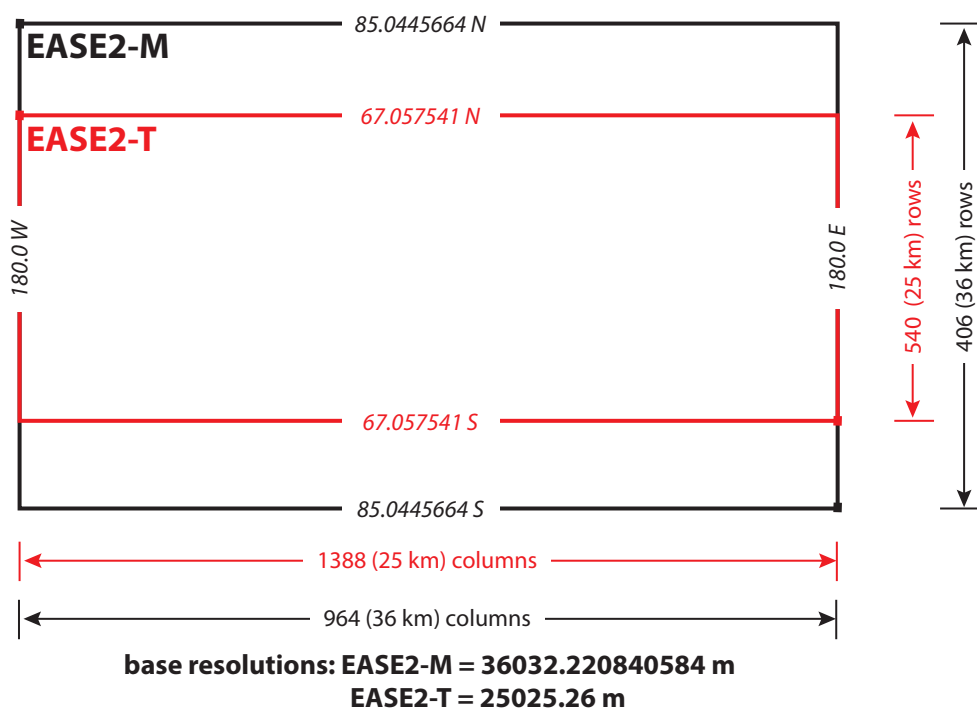
Figure 3: *Relationship of EASE-Grid 2.0 cylindrical projection extents. EASE2-T extent is defined for compatibility with CETB products. (Difference in latitudinal extent is exaggerated, see Fig. 2 for actual difference in projected extent.(Brodzik et al., 2021).*
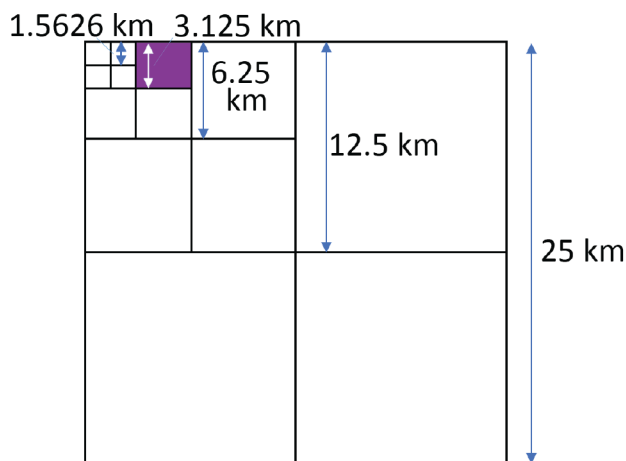
Figure 4: *CETB nested grids based on a 25 km base resolution cell. Only 25 km and 3.125 km divisions are used in SAR-SIR-SMAP products (Long et al., 2019).*

Table 5: *Available twice-daily* SAR-SIR-SMAP *radar image products.*

Type	days	Algo-rithm	Res. (km)	Re-gions[*]	Cor-rections	Polar-ations[†]	Size[††] N/S/T[*] (MB)
SAR	1	GRD	3.125	NST		HH,VV,XX	36/13/36
SAR	8	GRD	3.125	NST		HH,VV,XX	100/45/100
Slice	1	GRD	25	NST		HH,VV,XX	2/2/2.5
Slice	3	GRD	25	NST		HH,VV,XX	3/3/5
Slice	8	GRD	25	NS	Y	HH,VV,HV,VH	3/3/-
Slice	1	AVE	3.125	NST		HH,VV,XX	80/80/100
Slice	3	AVE	3.125	NST		HH,VV,XX	160/160/205
Slice	8	SIR	3.125	NS	Y	HH,VV,HV,VH	240/240/-
Footprint	1	GRD	25	NST		HH,VV,HV,VH	1.3/1.1/1.8
Footprint	3	GRD	25	NST		HH,VV,HV,VH	20/20/40
Footprint	1	SIR	3.125	NST		HH,VV,HV,VH	40/41/66
Footprint	3	SIR	3.125	NST		HH,VV,HV,VH	90/90/160

∗ Region code: N=Northern Hemisphere, S=Southern Hemisphere, T=Global
† XX=average cross-pol as provided by input SL1CS0 source for SAR. (HV+VH)/2 is used
in some slice images. (Product file names use HV.)
†† Representative. Actual sizes vary.

5   Algorithm Description

5.1   Background

Launched in January 2015, the SMAP spacecraft flies in a sun-synchronous polar orbit at inclination $98.1°$ and altitude $685\,\mathrm{km}$ (Piepmeier et al., 2016). The SMAP swath and scanning geometry (Fig. 5) produces a helical scan pattern on the surface with an along-track spacing of approximately 31 km between antenna rotations. While the radiometer employed the full one-way footprint, the radar footprint corresponds to the two-way 3-dB gain pattern whose footprint was approximately 18 km by 30 km.

The SMAP radar was unique that that three different kinds of radar measurements were collected simultaneously using a rotating pencil beam antenna. The measurement kinds differed in the way that the data was processed, which includes both real-time on board processing and ground processing. While SMAP slice and footprint measurements could be collected continuously over the full swath, SAR measurements are available only over part of the full swath, see Fig. 6. The relationship between the various measurement types is illustrated in Fig. 7.

The SMAP radar operated in quad polarization mode where it alternately transmitted vertical (V) and horizontal (H) polarizations, but received using both polarizations. It thus simultaneously collected cross-polarization measurements as well as like-polarization, i.e., HH, VV, HV, VH. In some cases the HV and VH measurements are combined, which is expressed as XX polarization.

The *effective* resolution of an image is defined by the *pixel spatial response function* (PSRF), where the effective resolution is given by the dimension(s) of one-half power (3-dB) extent of the PSRF. In contrast, the *measurement* response function (MRF) describes the spatial characteristics of the *individual* measurements. For a radiometer measurement, the MRF is a "smeared" version of the one-way antenna pattern where the smearing is due to the movement of the antenna pattern on the surface over the measurement integration period Long and Brodzik (2016a). For a radar measurement, the MRF depends on the two-way antenna pattern, the modulation, and the signal processing. For both radar and radiometer measurements, the PSRF depends on the MRF and the image formation algorithm.

In creating the SAR-SIR-SMAP radar image products, multiple measurements from different passes are combined into single pixel values. For SAR, the SAR image formation algorithm coherently (signal magnitude and phase) combines measurements to coherently estimate σ^o on a nominally 1 km grid (West, 2014). The resulting σ^o values are then re-gridded on to a 3.125 km grid using drop-in-the-bucket (DIB) techniques. The resulting SAR pixels have an effective resolution slightly coarser than the pixel spacing of 3.125 km. For slice and footprint measurements, the image formation process is inherently incoherent, i.e., the σ^o measurements (which are proportional to the signal power) are averaged. As a result, the effective resolution of the slice and footprint measurements is much coarser,
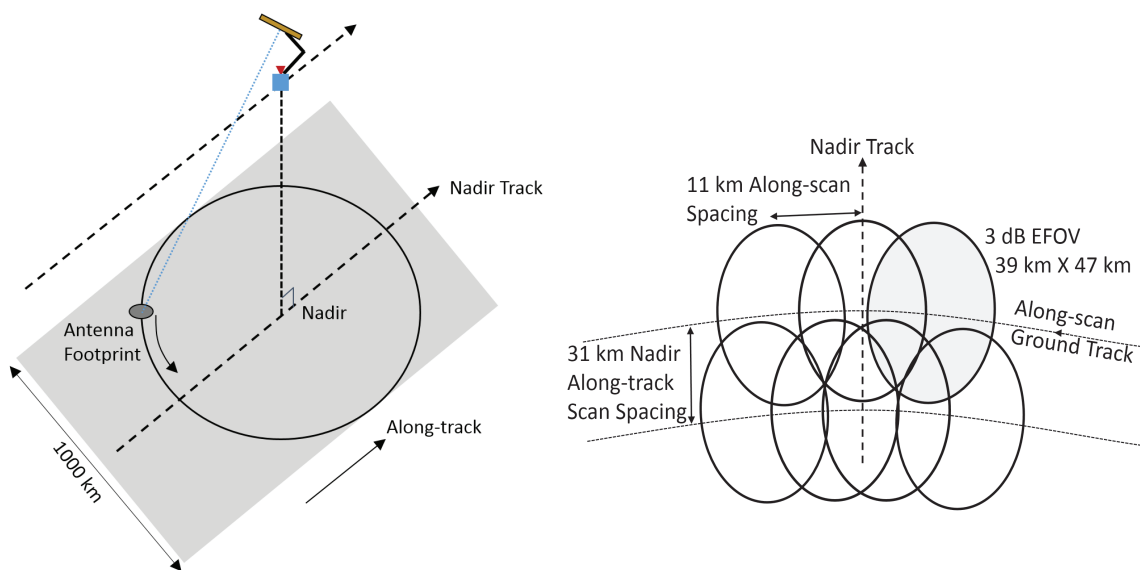
Figure 5: *Illustration of SMAP swath geometry (left) with antenna and feed rotation about the vertical axis. Incidence angle (not to scale) remains constant as the antenna scans the Earth surface. SMAP $3\,\mathrm{dB}$ antenna footprints (right) for sample measurements along two consecutive antenna rotations. Along-track footprint center spacing is approximately 31 km, with adjacent cross-track spacing approximately 11 km (Long et al., 2019).*
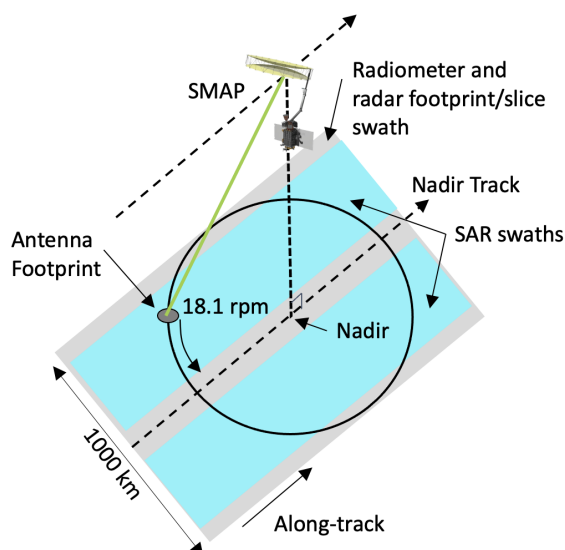
Figure 6: *SMAP swath layout. Radar footprint and slice and radiometer measurements are collected over a 1000 km swath. SAR measurements are not available over the central (nadir) portion of the swath.*

estimated to be ∼7 km and ∼12 km, respectively, even when resolution enhancement is applied.

We call the spacing of pixels the "pixel posting" or the "posting resolution". Note that the posting resolution is not necessarily the same as the effective resolution. In general, the effective resolution is coarser than the posting resolution (see (Long and Brodzik, 2016a)). In order to be compatible with the CETB data set, two posting resolutions are considered: 25 km and 3.125 km. See Fig. 8.

To create SMAP radar CETB-compatible products, the SAR measurements are re-gridded using DIB techniques on to a 3.125 km grid. For footprint and slice measurements, the SIR algorithm is applied on the same 3.125 km grid (but will have coarse effective resolution). In addition, DIB gridding is used to create σ^o images on 25 km grids for each measurement type. The SIR algorithm exploits the irregular patterns of measurement locations and signal oversampling (from overlaps in adjacent footprints and overlapping passes).

5.2   *SAR-SIR-SMAP* GRD Image Products

The *SAR-SIR-SMAP* products include both low-noise (low-resolution), fine resolution SAR, and enhanced-resolution data grids, each of which have different noise levels and effective resolutions. The various products have their advantages and disadvantages. The multiple images allow users the flexibility of choosing the appropriate images for their research
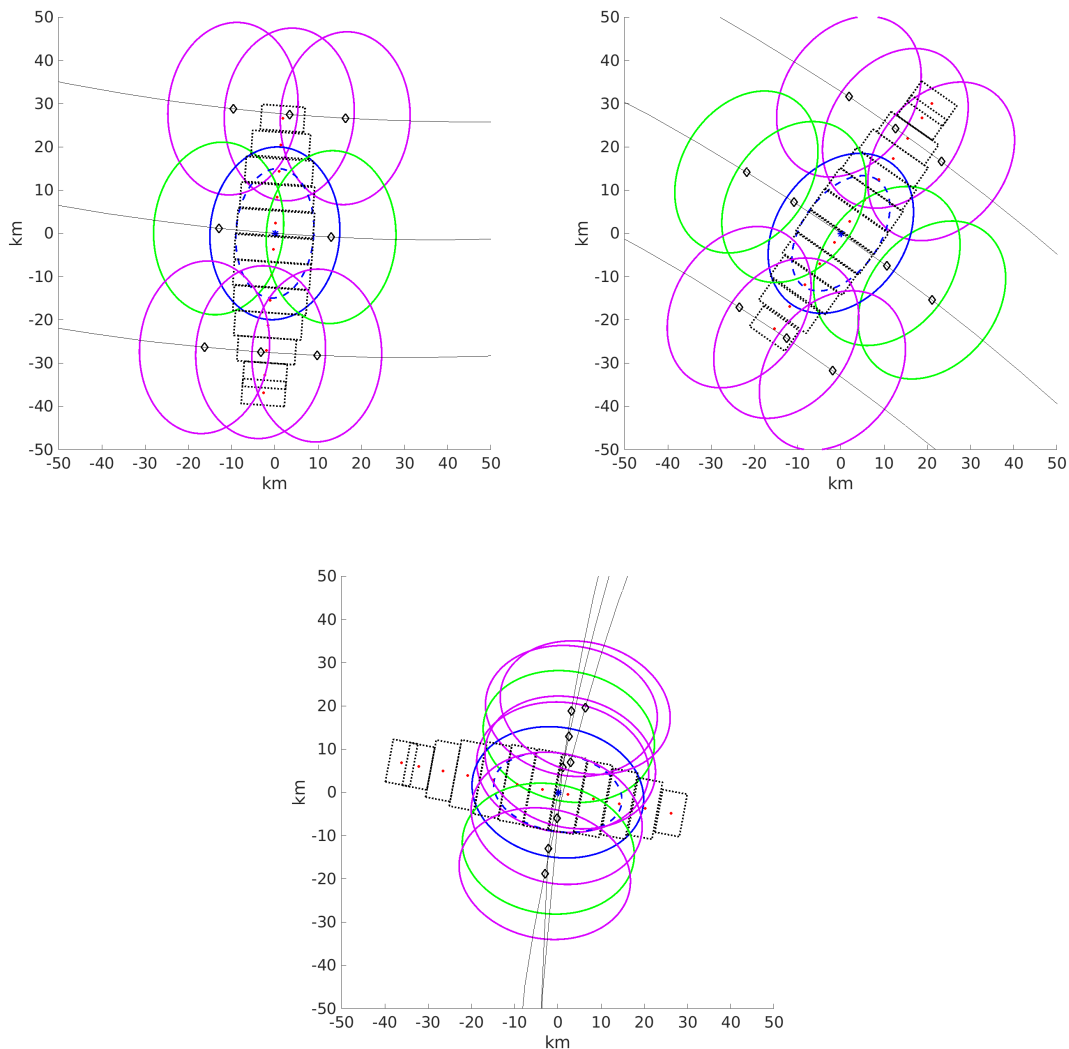
Figure 7: *Layout of the 3-dB outline of SMAP footprints and slices for different antenna rotation angles: (a) nadir swath, aft looking, (b) mid side swath, aft looking, (c) left-most swath. An asterisk at (0,0) is the center of the central measurement. Diamonds mark the locations of the footprint centers for consecutive pulses for three consecutive antenna rotations with lines indicating the path of the beam center. The large ovals correspond to the radiometer (one-way) footprints, with the central measurement in blue, adjacent pulses in green, and pulses from the previous and next rotation in magenta. The small blue dashed oval illustrates the radar (two-way) footprint for the central measurement. The dashed boxes illustrate the approximate slice responses which are centered at the red dots. Note that the slices extend significantly outside the two-way radar footprint. The bottom two and top slices have significantly higher K_p than the others are so are not included in image formation. SAR measurements are reported on a 1 km by 1 km map projection grid (not shown).*
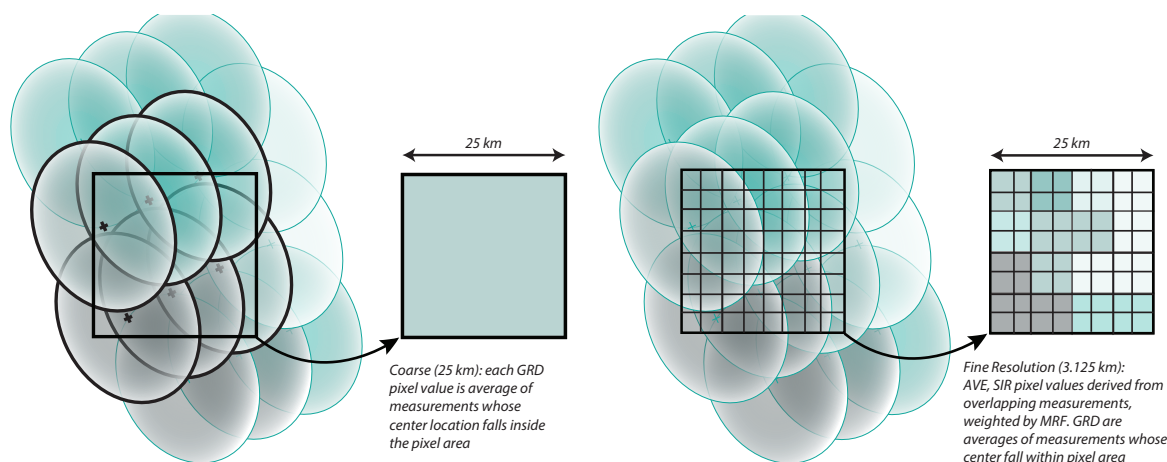
Figure 8: *Simplified illustration of coarse 25 km (left) vs. high resolution 3.125 km (right) pixels. DIB is used for SAR images on the high resolution pixels while AVE and SIR are used for high resolution slice and footprint images.*

application.

With three input measurement types (SAR, slice, and footprint), multiple imaging periods (1 day, 3 day, and 8 day), and two output resolutions (3.125 km and 25 km), different image formation algorithms are used as appropriate for each case. Table 5 summarizes the image product types. Simple GRD images are created using DIB techniques at 25 km and 3.125 km. In DIB, the measurements whose center falls within a given pixel area are averaged. AVE images use weighted averages where the weighting is the measurement MRF, which may vary from measurement to measurement. It is used for short-time slice images and for estimating scattering model parameters (see below). The SIR algorithm is employed for slice and footprint images on the 3.125 km pixel grid.

5.3 Radar Spatial Response and Image Reconstruction

The effective spatial resolution of an image product is determined by the spatial measurement response function (MRF) of the sensor and by the image formation algorithm used. The MRF is determined by the antenna gain pattern, the scan geometry (notably the antenna scan angle), and the signal processing (Long, 2017). The goal in forming a σ^o image map is to estimate the backscatter properties of the surface from noisy measurements that employ (possibly variable) MRFs that sample the surface. Though simple to implement, DIB techniques ignore the MRF, which limits their effective resolution. Reconstruction techniques that use the MRF can provide much finer effective resolution.

Reconstruction processing techniques effectively assume the underlying signal (the back-

scatter) being sampled is band-limited, which is the only consistent assumption possible with sampled data. For reconstruction, the backscatter at each point of a fine-scale pixel grid is estimated, producing a backscatter image or map. While the image is generated on a regular grid, the measurement locations and MRF are not aligned with the grid, and so the measurements form an irregular sampling pattern, which can complicate signal reconstruction.

An individual scatterometer backscatter measurement z_i can be modeled as the integral of the product of the MRF and the surface backscatter, i.e.,

$$z_i = \iint \mathrm{MRF}_i(x, y; pp) \sigma^o(x, y, \theta, \phi_i, t, pp) dx dy + \text{noise} \tag{1}$$

where $\mathrm{MRF}_i(x, y; pp)$ is the spatial MRF of the ith measurement at x, y and the surface σ^o depends on spatial location x, y, incidence angle θ, azimuth angle ϕ, time t, and polarization pp, i.e.,

$$\mathrm{MRF}_i(x, y; pp) = \iint \frac{G_a^2(x, y; pp) G_p(x, y; pp)}{R^4(x, y)}. \tag{2}$$

where

$$X = \iint \frac{G_a^2(x, y; pp) G_p(x, y; pp)}{R^4(x, y)} dx dy. \tag{3}$$

where $G_a(x, y; pp)$ is the effective two-way antenna gain at the surface at (x, y) for polarization pp, $G_p(x, y; pp)$ is the processor gain, and $R(x, y)$ is the slant range from the radar to the surface. Note that the measurement is an average of σ^o in spatial coordinates as well as in azimuth and incidence angles.

Eq. 1 is discretized on the imaging grid to become

$$z_i = \sum_{j \in \text{image}} h_{ij} a_j + \text{noise} \tag{4}$$

where a_j is the backscatter at the center of the jth pixel at (x_l, y_k) and $h_{ij} = MRF(x_l, y_k; \phi_i)$ is the discretely sampled MRF for the i-th measurement evaluated at the j-th pixel center where h_{ij} is normalized so that $\sum_j h_{ij} = 1$. In practice, the MRF is negligible some distance from the measurement center, so the sums need only be computed over a small area around the pixel. Ignoring the noise, Eq. 4 can be written as the matrix equation

$$\vec{Z} = \mathbf{H} \vec{a} \tag{5}$$

where $\mathbf{H}$ contains the sampled MRF for each measurement and $\vec{Z}$ and $\vec{a}$ are vectors composed of the measurements z_i and a_j, respectively. Even for small images, $\mathbf{H}$ is large and sparse, and may be over-determined or under-determined depending on the number and locations of the measurements. Reconstruction of the surface σ^o is equivalent to inverting Eq. 5.

The iterative SIR algorithm (Early and Long, 2001, Long et al., 1993) is a particular reconstruction algorithm that is specifically developed for scatterometer image formation. SIR approximates a maximum-entropy solution to an under-determined equation and a least-squares solution to an over-determined system. The first iteration of SIR is termed 'AVE' (for weighted AVErage) and provides a simple reconstruction estimate that is refined in later SIR iterations. The AVE estimate of the j-th pixel is given by

$$a_j = \frac{\sum_i h_{ij} z_i}{\sum_i h_{ij}} \tag{6}$$

where the sums are over all measurements that have non-negligible MRF at the pixel. The SIR iteration begins with an initial image a_j^0 whose pixels are set to the AVE values defined in Eq. 6. Thereafter, the iterative equation for single-variate SIR is given by

$$a_j^{k+1} = \frac{\sum_i u_{ij}^k h_{ij}}{\sum_i h_{ij}} \tag{7}$$

where

$$u_{ij}^k = \begin{cases} \left[\frac{1}{2p_i^k}\left(1 - \frac{1}{d_i^k}\right) + \frac{1}{a_j^k d_i^k} \right]^{-1} & d_i^k \geq 1 \\ \frac{1}{2}p_i^k(1 - d_i^k) + a_j^k d_i^k & d_i^k < 1 \end{cases} \tag{8}$$

$$d_i^k = \left(\frac{z_i}{p_i^k}\right)^{\lambda} \tag{9}$$

where $d_i^k = (s_i/p_i^k)^{\lambda}$ with $\lambda = \frac{1}{2}$. The factor d_i^k is the square root of the ratio of a measurement to its forward projection at the kth iteration. The update term u_{ij}^k is a non-linear function of both d_i^k and the previous image a_j^k. The sigmoid-like non-linearity in Eq. 8 constrains the amount of change permitted during any one iteration, thereby minimizing the effects of noise Long et al. (1993). Though not used in the production of these data, a spatial median filter can be applied to the image between iterations to further reduce the noise Long et al. (1993).

For scatterometers, SIR is implemented in dB (Long, 2017, Early and Long, 2001, Long et al., 1993); i.e., the computation is done on $10 \log_{10}(z_i)$ rather than on the linear-space value z_i as done in the radiometer version of SIR (Long and Brodzik, 2016a, Long and Daum, 1998). In considering the differences between linear and dB processing, recall the well-known fact that computing the arithmetic mean of values in dB is equivalent to computing $10 \log_{10}$ of the geometric mean of the linear-space values (Wikipedia, 2016). With the measurements in dB, the reconstruction processing can be viewed as a form of weighted geometric mean filtering. Since it has been found that geometric mean filters are better at reducing Gaussian-type noise and preserving linear features than (linear) arithmetic mean

filters (Pitas and Venetsanopoulos, 1986), some performance advantage to dB processing is expected and observed (Long, 2017). The linear and dB computations yield similar, but slightly different results, due to the relatively high signal-to-noise ratio (SNR) of the measurements and limited signal dynamic range.

In practice, since the σ^o measurements are quite noisy, attempting full image reconstruction can produce excessive noise enhancement. To reduce noise enhancement and resulting artifacts, regularization can be employed, at the expense of resolution (Long and Franz, 2016, Early and Long, 2001). Regularization is a smoothing constraint introduced in an inverse problem to prevent extreme values or over-fitting. Regularization results in partial or incomplete reconstruction of the signal (Long and Franz, 2016). It also creates a trade off between signal reconstruction accuracy and noise enhancement. SIR includes regularization achieved by prematurely terminating the iteration.

5.3.1   Local-Time-of-Day

As previously noted, the goal of image reconstruction is to estimate the surface σ^o from the sensor σ^o measurements. Measurements from multiple orbit passes over a narrow local-time-of-day window are combined. When multiple measurements are combined, the resulting images represent a temporal average of the measurements over the averaging period. There is an implicit assumption that the surface characteristics remain constant over the averaging period for both conventional-resolution (GRD) and enhanced-resolution (SIR) images.

The radar backscatter of natural surface is a strong function of the state of the water it contains, i.e., frozen or thawed. As a result of the SMAP sun-synchronous orbit geometry, the radar observations at a given location on the earth fall within two narrow diurnal windows. At the equator, these correspond to the ascending and descending orbit passes. The *SAR-SIR-SMAP* images on the cylindrical *EASE-Grid 2.0* projections are separated by ascending and descending passes.

Near the poles, the temporal windows widen to several hours but remain relatively narrow. Since surface temperatures can fluctuate widely during the day, daily averaging is not generally useful at these locations, since it smears diurnal temperature fluctuations in the averaged σ^o. However, it is reasonable to split the data into two distinct images per day, using intervals based on local-time-of-day (ltod), thereby only combining measurements with a similar ltod. This minimizes the fluctuations in the observed T_B at high latitudes due to changes in physical temperature from daily temperature cycling.

The *SAR-SIR-SMAP* images on the azimuthal projections are separated into twice-daily, morning and evening passes based on observation ltod. At low latitudes, which typically have few overlapping swaths at similar ltod in the same day, ltod division is equivalent to ascending/descending division. An ancillary data array is included in each file, to describe the effective time average of the measurements combined into the pixel for a particular
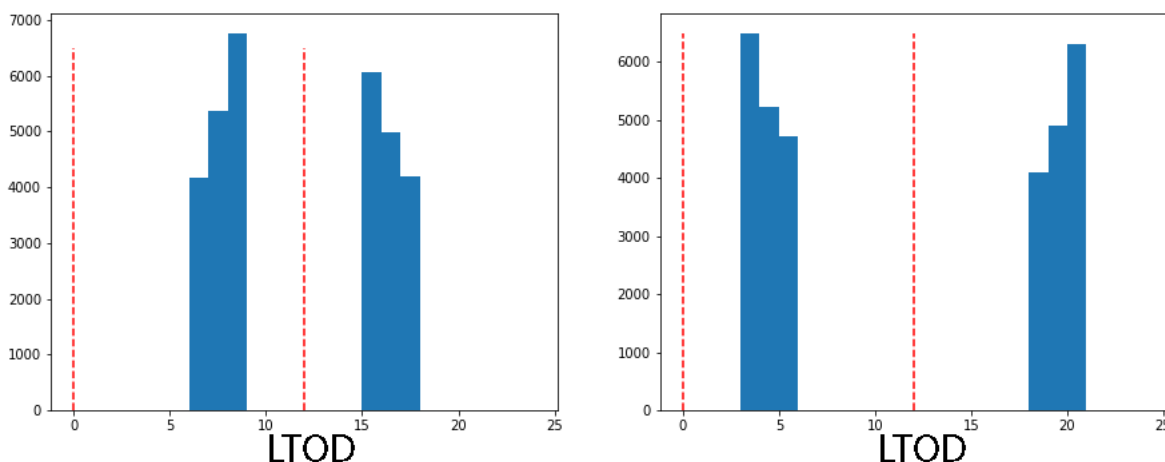
Figure 9: *Histograms of typical measurement ltod for SMAP radiometer measurements falling within a 1° latitude band at 70°–71° N (left) and 70°–71° S (right) for July 3, 2015. All measurements fall into only one of two narrow ltod time periods, centered at approximately 08:00 or 16:00 h in the Northern Hemisphere, and 04:00 or 20:00 h in the Southern Hemisphere. Although the center time varies with latitude, any point on Earth is observed at one of two times within ± 90 min of the times depicted here (Long et al., 2019).*

day. This enables investigators to explicitly account for the ltod temporal variation of the measurements included in a particular pixel.

Histograms of the ltod SMAP radiometer measurements falling within two narrow high-latitude bands ($\pm$70–71) are shown in Fig. 9. For the SMAP platform orbital position, a natural division in the measurement ltod is at 00:00 and 12:00 h. For consistency with Long and Brodzik (2016b) and Brodzik et al. (2021), the *SAR-SIR-SMAP* data are produced using this ltod division. Note how the ltod falls within one of two tight groups that correspond to the ascending and descending orbit passes, and that there are natural divisions in the measurement ltod at 00:00 and 12:00 hrs. Thus, the measurements provide twice-daily sampling. Note that when more than day's worth of data, the ltod division is maintained so that a multi-day morning image combines only morning observations.

5.4   Sample Data

Figure 10 contains sample subsets of *SAR-SIR-SMAP* data extracted from the full *EASE-Grid 2.0* Northern Hemisphere grid for different measurement types and processing resolutions for comparison purposes. Visual comparison of the images reveals improved detail in the SIR images compared to the DIB GRD images. Of course, the fine resolution SAR images provide the finest detail, but SAR images are not available in all locations, so SIR images must be used in these cases. A second comparison is provided in Fig. 12.

For considering the performance of the AVE and SIR reconstructions, the 3.125 km SAR image is used as a reference since it has the highest effective spatial resolution. Figure 12 compares the various images. Difference statistics are computed for pixels over land and shown in Tab. 6. Unsurprisingly, the GRD images, which have the greatest averaging, but lowest resolution, have the smallest differences, while the SIR images, which exhibit finer detail have differences with SIR Slice having the smallest errors of the reconstruction images.

Table 6: *Summary difference statistics compared to 8 day 3.125 km reference SAR image. Computed in dB. Only pixels falling over land used.*

days	Measurement type	Algorithm	mean	STD
3	Footprint	GRD	0.158	0.435
3	Slice	GRD	0.111	0.316
3	Footprint	SIR	0.706	3.428
3	Slice	AVE	0.588	3.278
8	Slice	SIR	0.368	1.965
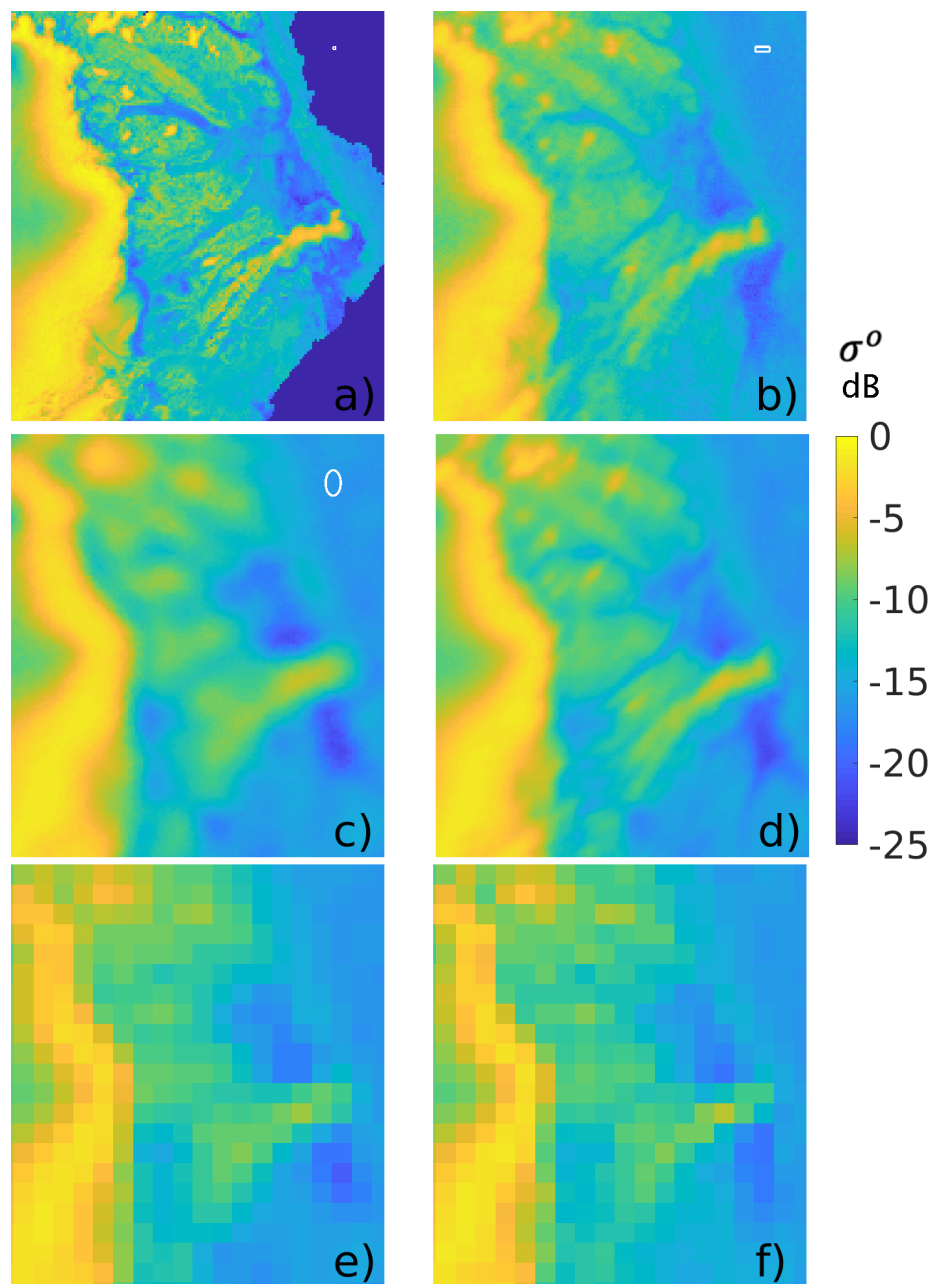
Figure 10: *Product comparison examples showing σ^o in dB for a zoom in area in northeast Greenland. (a) 3.125 km SAR GRD, (b) 3.125 km Slice SIR, (b) 3.125 km Footprint SIR, (c) 3.125 km Slice AVE, (d) 25 km Footprint GRD, (e) 25 km Slice GRD. The small white box in (a) shows the size of a 3.125 km pixel, the SAR resolution. The small white rectangle in (b) represents the size of a typical slice. The white oval in (c) is the size of the two-way radar footprint.*
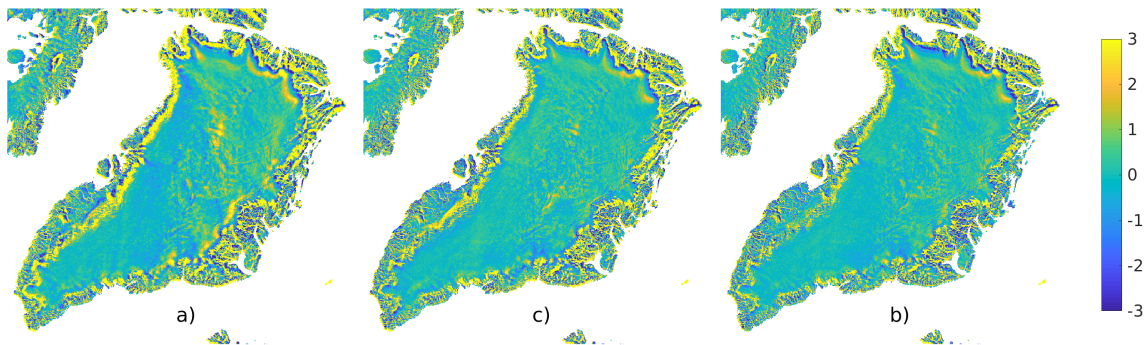
Figure 11: *σ^o difference images over land between algorithm image and 3.125 km SAR reference image. (a) 3 day SIR Footprint. (b) 3 day AVE Slice. (c) 8 day SIR Slice. Images have been land masked. Difference statistics are summarized in Tab. 6.*
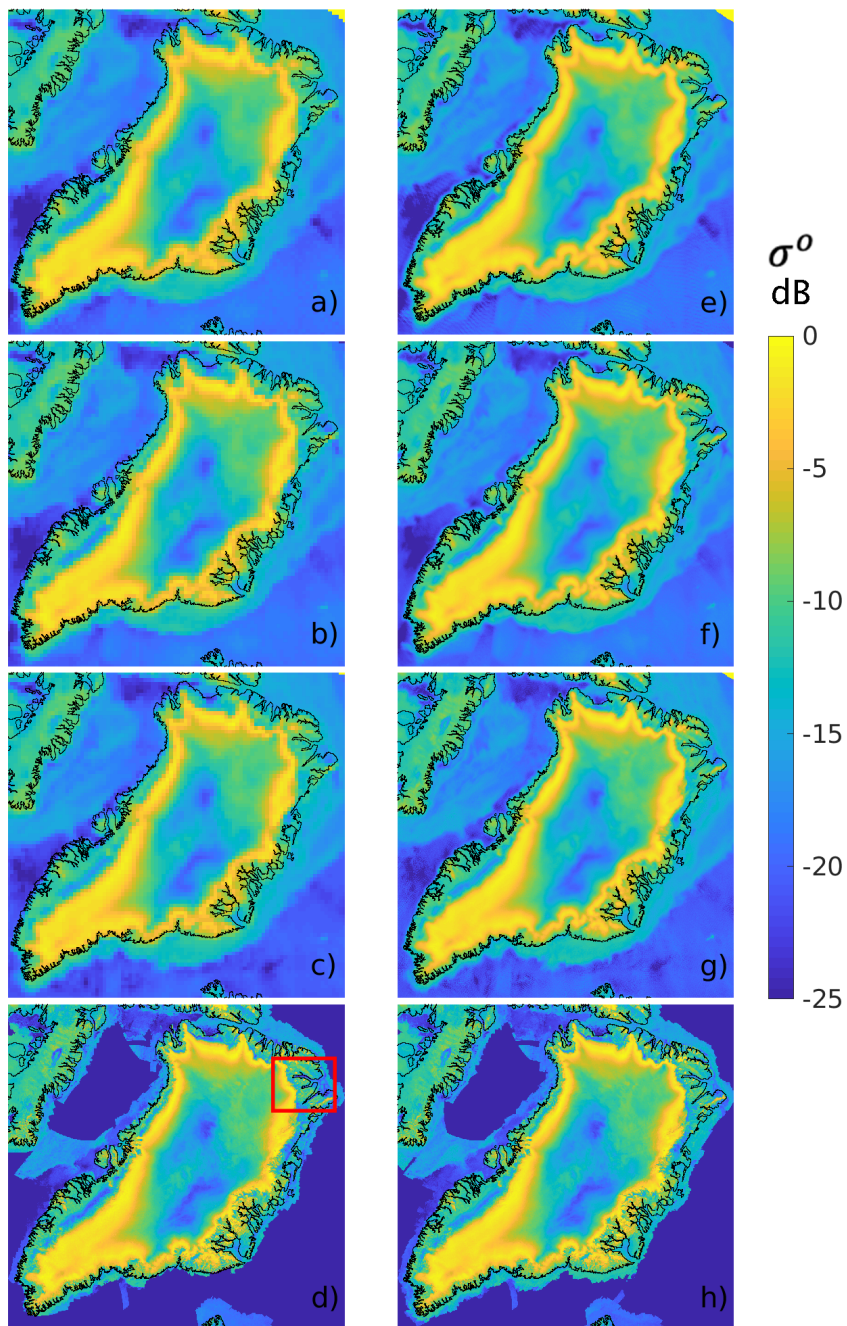
Figure 12: *Evening LTOD, HH pol σ^o images at different resolutions from different measurement types. a) 3 day Footprint 25 km GRD. b) 3 day Slice 25 km GRD. c) 3 day SAR 25 km GRD. d) 3 day SAR 3.125 km GRD. e) 3 day Footprint 3.125 km SIR. f) 3 day Slice 3.125 km AVE. g) 8 day Slice 3.125 km SIR. h) 8 day SAR 3.125 km GRD. At the printed resolution, it is difficult to see the difference in the images. Zoom-in area comparisons are given in Figs. 10 and 13.*

6 Measurement Modeling

To dive deeper into the SMAP radar data and the performance of the imaging algorithms, we define some small study regions in the Greenland Ice Sheet, see Fig. 13. The regions are individually small enough to have nearly constant scattering characteristics, but span the range of ice facies over the ice sheet with a variety of mean σ^o values. The location of a section line across the ice sheet is also shown, with a plot of σ^o versus displacement from the center of the line shown in Fig. 14 for each of the major σ^o products. Each of the imaging algorithms has its advantages and disadvantages. In Fig. 14 the algorithms track each other closely, except beyond 500 km. At this point, the SAR coverage does not extend far enough out to include sea ice of the east coast, whereas the slice and footprint images do cover this area. One of the advantages of the slice and footprint images over the SAR images are their coverage On the other hand, over the ice sheet the very fine resolution of the SAR image shows some dips and peaks in σ^o that are not fully represented by the coarser resolution of the slice and footprint images, particularly in the highly variable near-coastal area between 300 km and 500 km. While the resolution differences probably account for most of the differences, there may be contributions due to the higher noise level of the SAR images compared to the slice and footprint images.
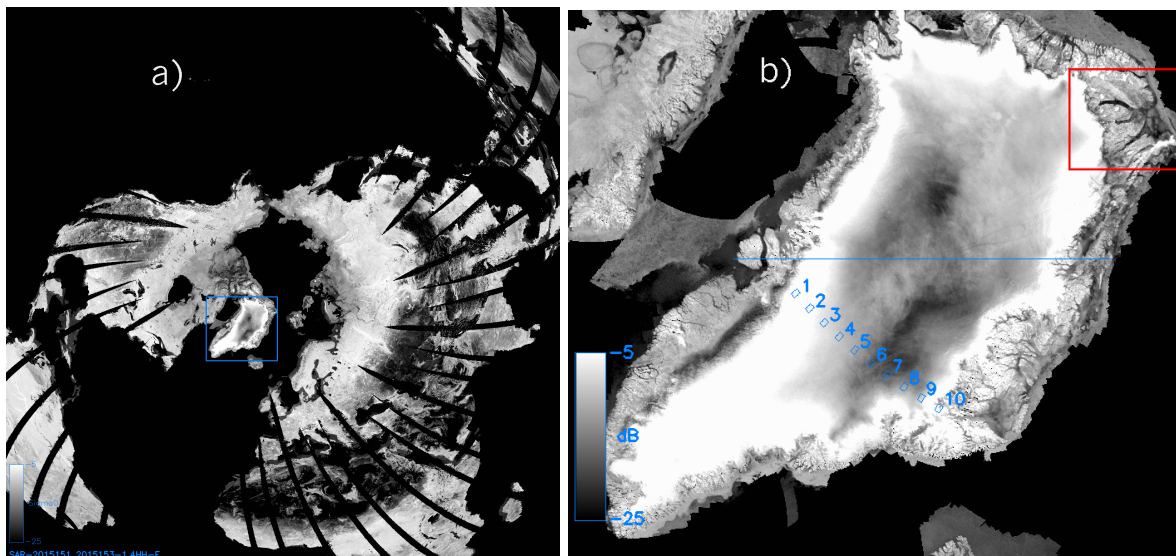
Figure 13: *(a) 3 day evening, HH pol SAR image of the Northern Hemisphere with Greenland study area indicated. (b) Zoom in of (a) showing the location of 10 sub areas as small boxes and a horizontal line segment showing the location of line section plotted in Fig. 14.*
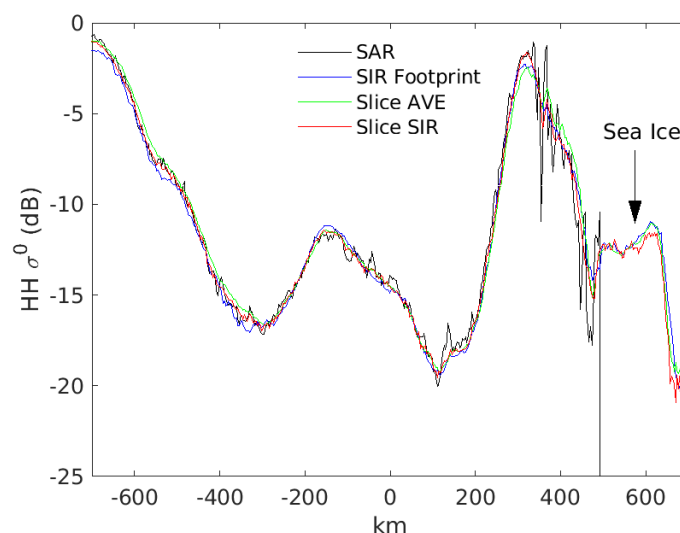
Figure 14: *Plot of evening LTOD, HH σ^o for various image products versus distance along an arbitrary line section crossing Greenland. See Fig. 13 for map of line location. Note that the SAR data does not extend far from the coast and so does not cover the full extent of sea ice off the east coast.*

6.1   Incidence Angle Effects

Over natural surfaces σ^o depends on the measurement incidence angle. Due to careful control of the SMAP spacecraft attitude, the incidence angle of the center of the antenna footprint by varies by less than $1°$ over the orbit. However, within the footprint, the incidence angle varies by $\pm 2°$. Within the footprint is also a small variation ($<0.5°$) in azimuth angle, but this is considered negligible. The incidence angle variation within the footprint affects both the SAR and the slice measurements since they resolve the antenna footprint into many individual smaller areas that have different mean incidence and azimuth angles that are reported in the respective data products. In contrast, footprint measurements integrate the echo return over the full footprint and report a single σ^o, mean incidence angle, and mean azimuth angle value. In effect, footprint measurements average out the incidence angle dependence. To illustrate this, Figs. 15-17 show the variation in incidence angle for measurements collected over each of the Greenland study regions for SAR, slice, and footprint measurements, respectively, during an 8-day interval. Note the higher variability in σ^o in the SAR observations (Fig. 15) compared to the slice and footprint cases in Figs. 16 and 17. This is attributed mainly to the higher noise level of the SAR measurements compared to the lower resolution (and, thus, more averaged) slice and foot measurements.

Noting the sloping dependence of σ^o with incidence angle, for the SAR and slice cases separate linear fits of σ^o versus incidence angle were determined using σ^o expressed in dB
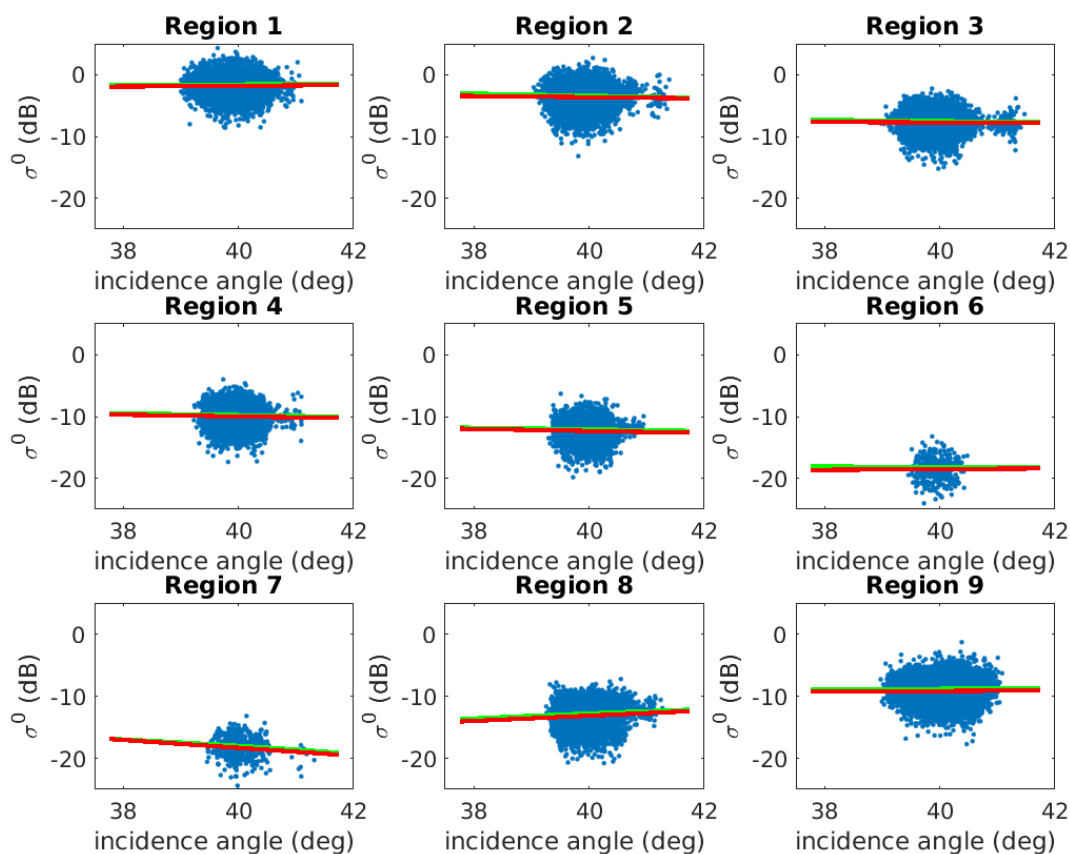
Figure 15: *Evening LTOD, HH SAR σ^o versus incidence angle for each sub area (see Fig. 13) showing linear (g) and dB (r) model fits.*

and as a non-log (linear units) value in Figs. 15-17. Note that over the study regions both positive and negative slopes were observed (see the B value in right column of Tab. 7). We further note that for footprint measurements, the incidence angle variation is too small to make a reliable slope estimate, and so the slope, denoted by B is treated as zero.

The incidence angle normalization $\gamma^o = \sigma^o / \cos\theta$ where θ is the incidence angle is commonly used. However, the slope of this correction is strictly downward and since upward slopes are observed in many areas, this normalization is not used. Instead, a linear slope is used which is felt to be adequate for quantifying and correcting for incidence angle variations over the narrow range of incidence angles of the SMAP measurements.

Table 7: *Values of M124 Model Coefficients for Each Greenland Study Region for Each Measurement Type*

Type/ Region	M124 Model Coefficient Values							
	A_0 dB	A_1 dB	P_1 deg	A_2 dB	P_1 deg	A_4 dB	P_4 deg	B db/deg
SAR								
1	-1.71	0.564	85.4	0.072	129.2	0.043	90.3	+0.043
2	-3.58	0.277	105.0	0.064	-151.7	0.045	-37.2	-0.027
3	-7.69	0.278	147.0	0.087	-13.7	0.093	-22.8	-0.036
4	-9.97	0.165	130.5	0.046	-23.2	0.103	45.4	+0.074
5	-12.35	0.081	54.5	0.160	-46.5	0.059	64.4	+0.053
6	-18.64	0.455	59.4	0.184	75.6	0.223	-156.7	-0.088
7	-18.24	0.308	-143.1	0.784	-80.0	0.457	35.9	+0.268
8	-12.95	0.746	-173.8	0.353	95.9	0.059	-169.8	-0.010
9	-9.16	0.526	117.8	0.278	112.9	0.138	-83.1	-0.137
Slice								
1	-1.69	0.395	92.0	0.102	-104.2	0.264	92.1	+0.264
2	-4.27	0.146	105.2	0.097	-61.3	1.110	-88.8	-1.110
3	-10.09	0.311	133.6	0.136	-78.7	0.492	-78.4	-0.482
4	-13.28	0.236	136.3	0.177	-83.9	0.719	-99.5	-0.709
5	-16.28	0.183	57.5	0.162	-74.6	0.683	-68.3	-0.635
6	-20.67	0.389	18.4	0.041	-80.7	0.549	-79.5	-0.540
7	-20.05	0.324	161.8	0.177	3.9	0.445	155.8	+0.183
8	-15.65	0.929	-168.9	0.347	7.1	0.904	-171.5	-0.134
9	-10.81	0.665	58.0	0.319	167.3	2.234	129.2	+1.730
Foot								
1	-1.59	0.529	87.8	0.054	153.1	0.210	136.0	0.000
2	-3.18	0.296	94.8	0.044	167.9	0.450	-26.7	0.000
3	-7.35	0.298	127.3	0.094	-82.1	0.185	-50.5	0.000
4	-9.59	0.149	114.2	0.101	-151.0	0.232	-54.0	0.000
5	-12.03	0.121	20.7	0.070	+13.8	0.244	-22.4	0.000
6	-17.22	0.234	33.7	0.044	-79.7	0.243	-24.9	0.000
7	-17.73	0.203	175.9	0.120	-61.2	0.305	-123.9	0.000
8	-12.99	0.366	-160.5	0.389	-30.4	0.233	-159.4	0.000
9	-8.09	0.520	127.7	0.308	-166.7	0.817	-171.9	0.000
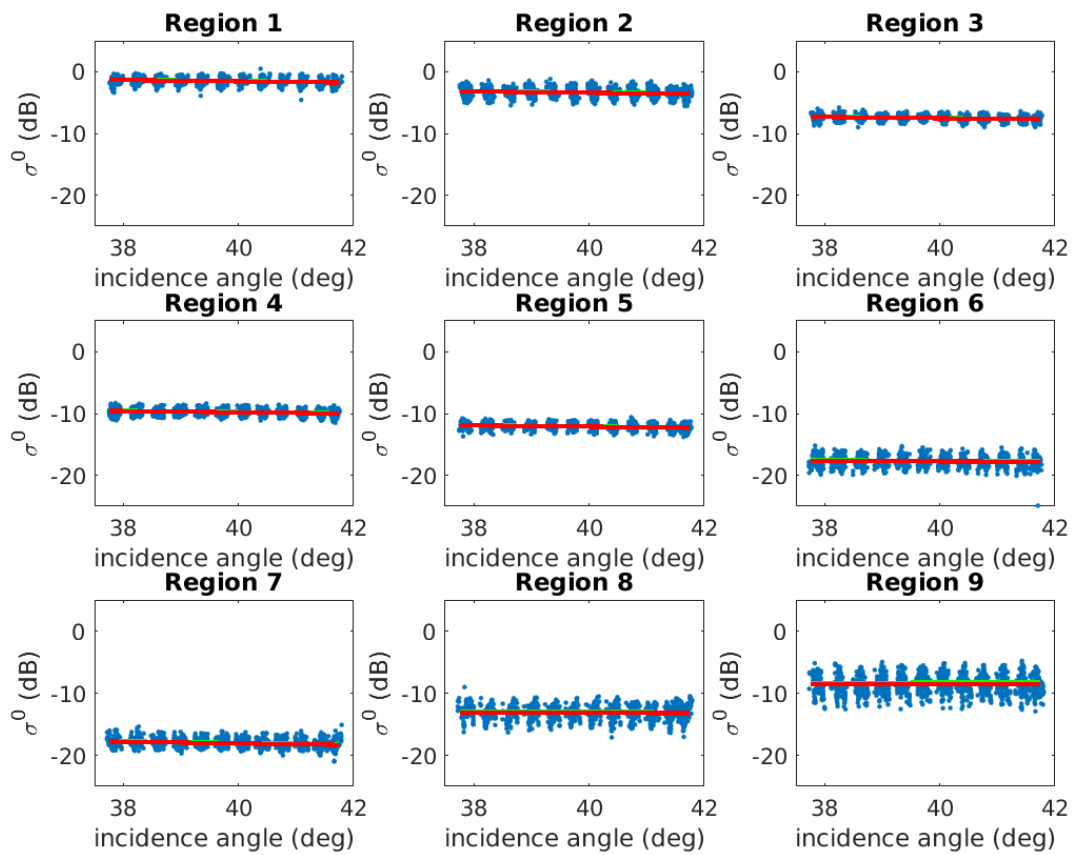
Figure 16: *Evening LTOD, HH slice σ^o versus incidence angle for each study region showing linear (g) and dB (r) model fits.*
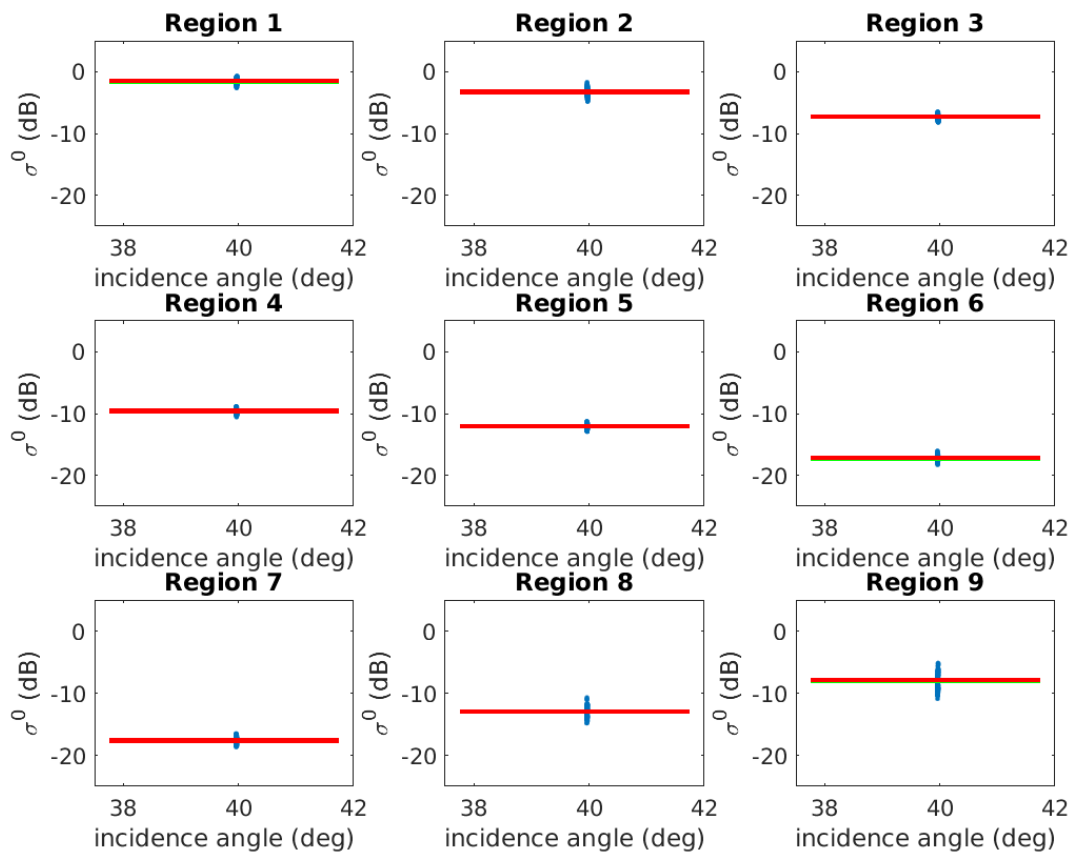
Figure 17: *Evening LTOD, HH footprint σ^o versus incidence angle for each study region showing linear (g) and dB (r) model fits.*

6.2   Azimuth Angle Effects

Periodic natural surfaces exhibit variations in σ^o with azimuth angle. Because the SMAP radar employed a rotating pencil beam antenna, over the course of the orbit's 8 day repeat cycle each point on the surface could be observed at multiple azimuth angles. For example, as the spacecraft passes over a particular location within the swath, the location is first observed looking, then a short while later the same location is observed looking backward. Over the 8 day orbit repeat cycle, the ground track shifts so that the same location is observed from a different set of azimuth angles for each pass. The precise distribution of azimuth angles depends on the orbit latitude, with the narrowest range near the equator and the largest range at high latitudes. This multiple azimuth angle capability provides a unique opportunity to study the azimuth angle variation of σ^o at L-band. Note that there is a trade off between the time period and the azimuth sampling. Short time periods provide better temporal resolution for tracking sea ice motion and rapid freeze thaw events. However, short time periods provide inadequate coverage and/or azimuth sampling to reliably estimate the azimuth angle variation, particularly when the data is divided by local time of day. Because an 8 day period provides the maximum azimuth angle sampling, this period was used in the study when estimating and compensating for azimuth and incidence angle effects. To support studies requiring better temporal resolution that can ignore azimuth angle variation, we also created selected image products with 1-day and 3-day periods. In creating a time series of times, a "moving average" approach was used with overlapping imaging periods, that start every mission day and extend through the desired 1-, 3-, or 8-day period (or to the end of the mission, whichever comes first).

Note that a particular σ^o observation is an average of σ^o in spatial coordinates as well as in azimuth and incidence angles. The azimuth angle span for a given measurement is small and can be neglected. On the other hand, the variation in σ^o as a function of azimuth angle for different measurements is important and can provide useful geophysical information, e.g., wind over the ocean (Meissner and Wentz, 2017), snow dunes and sastrugi (Long and Drinkwater, 2000, Ashcraft and Long, 2006), and sand dunes (Stephen and Long, 2007). Since each satellite pass observes a given point on the surface from a limited azimuth angle, the variation of σ^o with azimuth can lead to biases in the mean σ^o value and to imaging artifacts when multiple passes with different azimuth angle observations are combined. To deal with azimuth variation of σ^o on the GI, previous investigators (e.g., (Long and Drinkwater, 2000, Ashcraft and Long, 2006, Lindsley and Long, 2016)) used a Fourier series model for the azimuth variation observed in σ^o. Following their work, we use a similar approach for modeling the azimuth variation of σ^o. This technique, while applied globally, is most useful over the GI in the polar regions. Over the ocean and over other land areas, the amplitude of azimuth angle variation is very small and the directional angle estimates reveal swath-related artifacts.

Figures 18-20 show the variation in σ^o versus azimuth angle for of the Greenland study
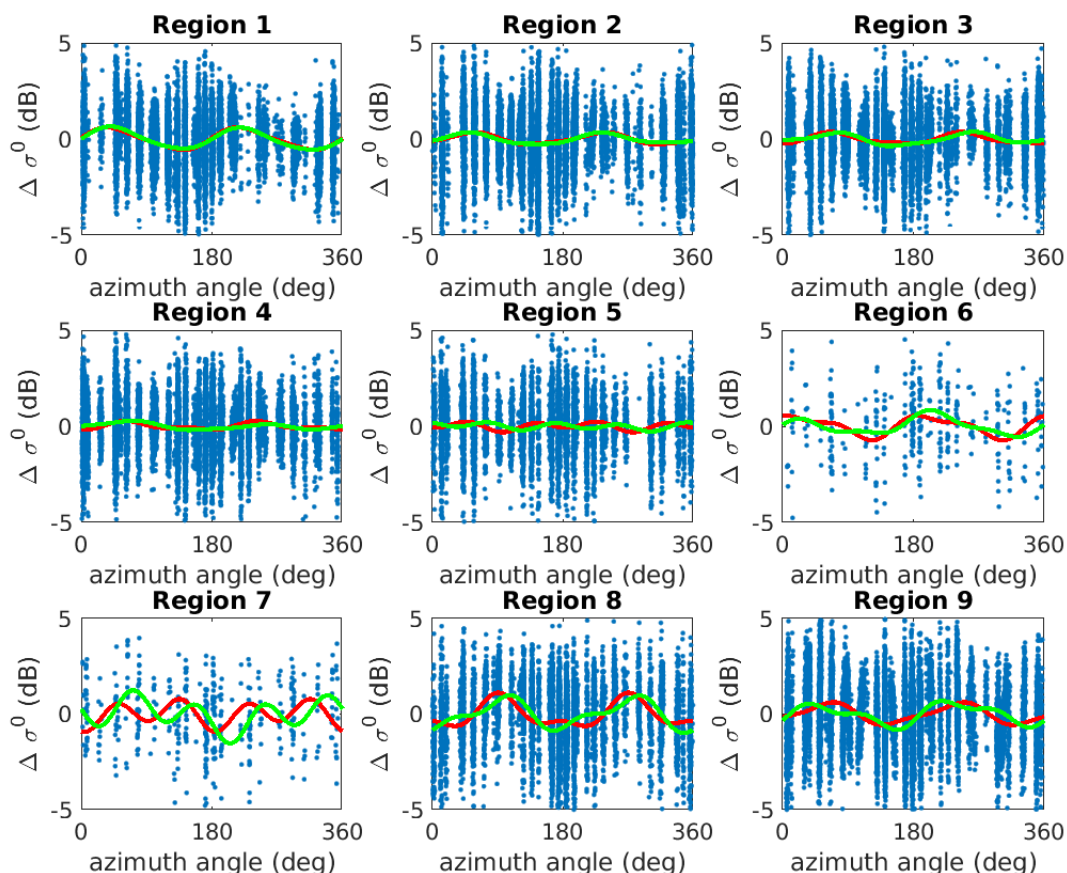
Figure 18: *Evening LTOD, HH SAR σ^o versus azimuth angle for each study region and MI124 (g) and MI24 (r) model fits.*

regions for SAR, slice, and footprint measurements, respectively. The σ^o have been corrected for incidence angle using the fits determined in Figures 15-17. Note the higher variability in σ^o in the SAR observations compared to the slice and footprint cases. This is attributed mainly to the higher noise level of the SAR measurements compared to the lower resolution (and, thus, more averaged) slice and foot measurements. Also note the declining number of measurements as the measurement resolution is coarser. All the cases exhibit a smoothed variation with azimuth angle of: less than 1 dB for SAR and footprint measurements and up to 3 dB for slice measurements. Note that the variation of σ^o is generally well described by simple harmonic models.
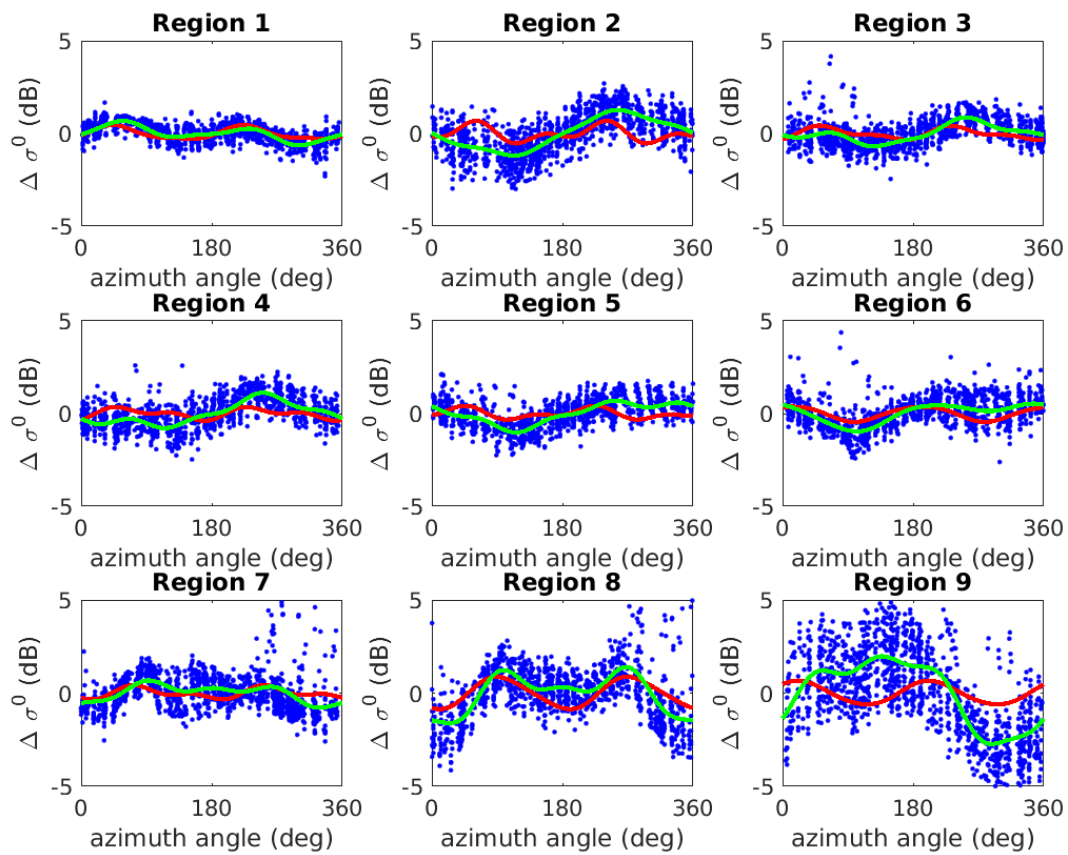
Figure 19: *Evening LTOD, HH slice σ^o versus azimuth angle for each study region and MI124(g) and MI24 (r) model fits.*
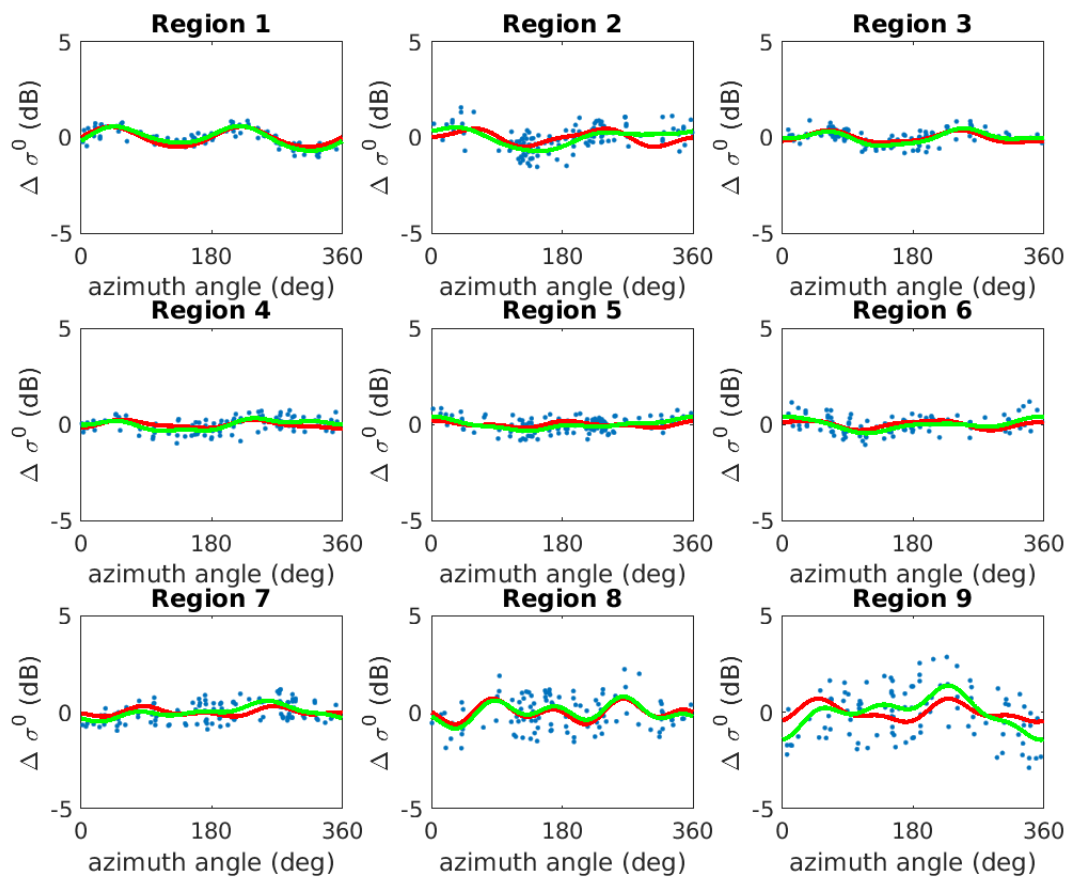
Figure 20: *Evening LTOD, HH footprint σ^o versus azimuth angle for each study region and MI124 (g) and MI24 (r) model fits.*

6.3 Incidence/Azimuth Models

To account for the azimuth modulation behavior, the observed σ^o is modeled as

$$\sigma^o = A_0 + B(\theta - 40°) + A_1\cos(\phi + P_1) + A_2\cos(2\phi + P_2) + A_4\cos(4\phi + P_4) \qquad (10)$$

where A_0 is the mean σ^o; B is the slope of σ^o versus incidence angle θ normalized to 40°; ϕ is the azimuth angle of the radar illumination relative to north; and A_1, A_2, and A_4 are the amplitudes and P_1, P_2, and P_4 are the phases of the first, second, and fourth order azimuth modulation terms. Table 7 lists the values of the scattering model coefficients for each of the small Greenland study regions. We note that significant azimuth variation is common over the GI, but is only rarely observed elsewhere over large regions.

At each pixel, the model parameters A_0 (the mean σ^o), B (the normalized slope of σ^o versus incidence angle, A_1 (the magnitude of the first order azimuth modulation), P_1 (the phase angle of the 1st order azimuth modulation), A_2 (the magnitude of the second order azimuth modulation), P_2 (the phase angle of the 1st order azimuth modulation), A_4 (the magnitude of the fourth order azimuth modulation), and P_4 (the phase angle of the 1st order azimuth modulation) are estimated from slice measurements. These values are reported in the slice products. Examples of these values for Antarctica and Greenland are shown in Figs. 21 and 22, respectively. Note the greater mean azimuth variation in Antarctica relative to Greenland. Table 7 lists the values of the the scattering model coefficients for each of the Greenland study regions. Table 8 summarizes the statistics of the model fit for different model orders.

The various models are denoted by M for mean-only (i.e., only A_0 used, with other values treated as zero); MI for mean and incidence angle (i.e., only A_0 and B are used); MI24 that includes mean, incidence angle dependence, and second and fourth order azimuth terms (i.e., A_0, B, A_2, P_2, A_4, and P_4) and MI124 which includes all the parameters.

In Figs. 18-20 we observe that most of the azimuth variation is covered using only second- and fourth-order terms (the red curve), though some regions (notably 8 and 9) benefit from including a first-order sinusoidal term (the green curve). Given the relatively small variation of the model parameters since in these figures, the M model is used in SAR and footprint cases, i.e., the azimuth variation is ignored in image formation for processing these measurement types. Azimuth modeling is only included in processing slice measurements. Because the magnitude of the A_1 is nominally small for most areas and including in the fit increases the estimate noise, we adopt the MI24 for slice SIR processing. For each measurement, the pixels for which the measurement's MRF is non-negligible are determined. Then, for each pixel the MI24 model parameters are determined using least-squares estimation. The resulting model parameter images are median filtered using a 3×3 median filter to eliminate spike artifacts that arise due to occasional inadequate observations that span the full range of possible azimuth and incidence angles. The resulting MI24 model parameter images are shown in Figs. 21 and 22. The MI24 model parameter images are included as ancillary images in the slice product files.

Table 8: *RMS difference between the σ^o measurements and model fits for each study region and measurement type*

Type/ Region	Count	Model M	MI	MI24	MI124
SAR	**63599**	**1.53**	**1.52**	**1.51**	**1.51**
1	10905	1.35	1.35	1.30	1.30
2	12030	1.50	1.51	1.49	1.49
3	10656	1.41	1.40	1.40	1.39
4	8956	1.43	1.44	1.43	1.43
5	5823	1.51	1.51	1.52	1.50
6	378	1.74	1.73	1.71	1.71
7	453	1.70	1.71	1.79	1.74
8	5590	1.82	1.78	1.78	1.77
9	8808	1.79	1.77	1.75	1.76
Slice	**10786**	**1.17**	**1.15**	**1.14**	**1.46**
1	1261	0.46	0.51	0.42	0.60
2	1221	1.11	1.13	1.10	1.63
3	1195	0.70	0.72	0.70	0.79
4	1108	0.79	0.81	0.83	1.04
5	1145	0.75	0.79	0.75	0.92
6	1178	0.84	0.80	0.79	1.01
7	1299	1.05	1.03	1.05	1.05
8	1153	1.40	1.28	1.27	1.26
9	1226	2.29	2.26	2.25	3.11
Foot	**1023**	**0.65**	**0.68**	**0.69**	**0.75**
1	105	0.46	0.56	0.57	0.61
2	127	0.66	0.75	0.74	0.80
3	121	0.37	0.44	0.43	0.39
4	102	0.39	0.41	0.43	0.40
5	130	0.37	0.37	0.38	0.43
6	100	0.45	0.49	0.48	0.52
7	122	0.52	0.53	0.53	0.56
8	110	0.85	0.87	0.89	0.91
9	106	1.28	1.27	1.32	1.53
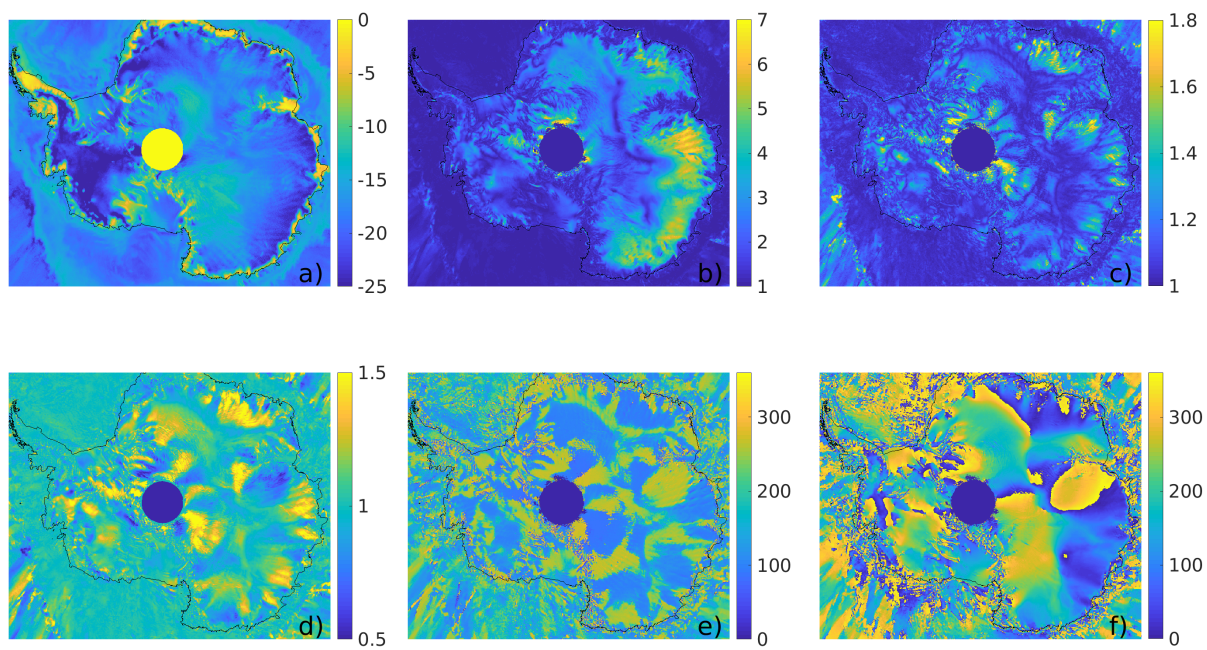
Figure 21: *Plot of evening LTOD, HH evening σ^o azimuth and incidence angle variation images for Antarctica. (a) Mean σ^o, (b) A_2, (c) A_4, (d) B, (e) P_1, (f) P_2.*
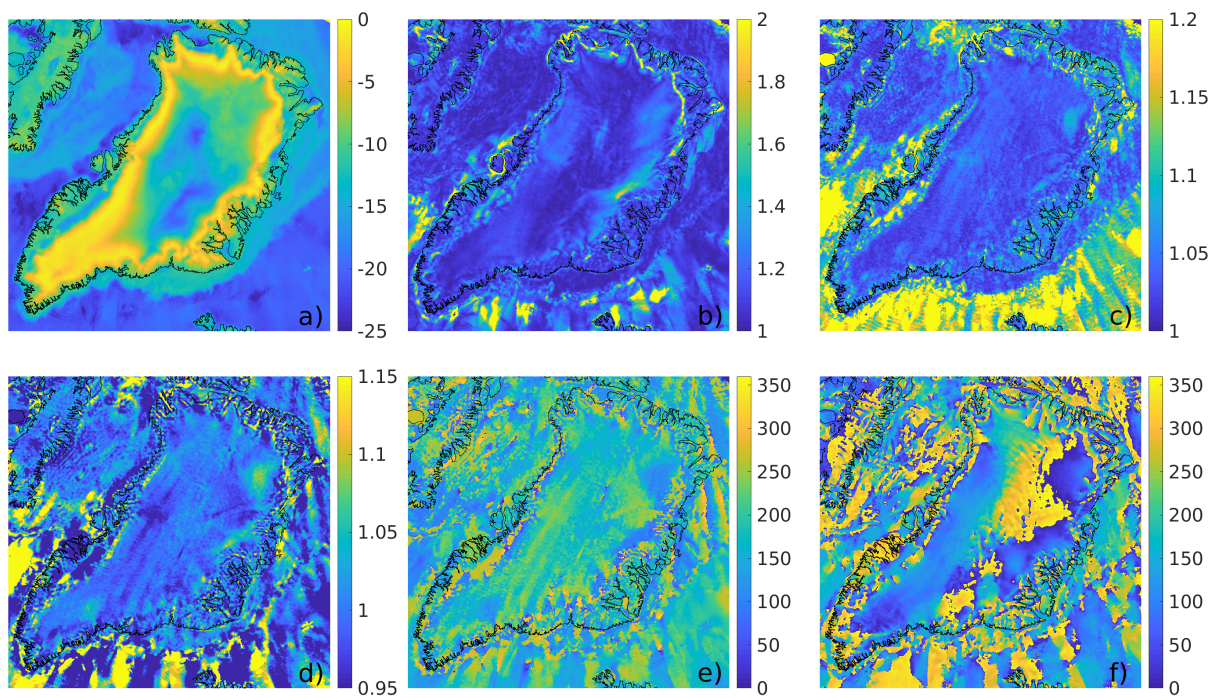
Figure 22: *Plot of evening LTOD, HH σ^o azimuth and incidence angle variation images for Greenland. (a) Mean σ^o, (b) A_2, (c) A_4, (d) B, (e) P_1, (f) P_2.*

6.4   Model-Based Correction

The net effect on σ^o due the azimuth and incidence angle variations is up to several dB for an individual measurement. Since multiple measurements from different azimuth and incidence angles are averaged when creating images, however, the effects of the angle variations on the averaged pixel σ^o tend to be small, though image artifacts can be observed in short time images. Such artifacts can be minimized by using the model parameters to adjust or correct for the measurement geometry. The limited information in the footprint measurements regarding incidence angle and the limited understanding of the effects of the SAR processing on the azimuth processing, prevent us from reliably applying the incidence/azimuth models to the SAR and footprint measurements. Hence, the M model used in the SAR and footprint cases corresponds to the mean σ^o value. However, the slice measurements are well suited for simultaneously estimating the incidence and azimuth angle dependence and so can employ the correction strategy. To ensure consistency with the SAR and footprint cases, rather than report the estimated model A_0 value, the other model coefficients are employed to compute a correction factor that is applied to the individual measurements prior to image formation. The corrected mean σ^o image is then reported.

To correct for the azimuth and incidence angle of a particular measurement, the weighted forward projection of each measurement is first computed from the estimated MI24 model parameter images using the measurement's MRF. In this computation the A_0 term is not included. The estimated σ^o variation due to the azimuth and incidence angle is subtracted from the σ^o measurement, yielding a "corrected" measurement. The corrected measurement is then used for computing the GRD or SIR images of the mean σ^o . This approach provides the higher resolution σ^o images than merely using the original MI24 A_0 model value. The resulting correctedσ^o image has fewer artifacts than an uncorrected image. Figure 23 shows a SIR image computed from corrected slice σ^o measurements and a difference image between corrected and uncorrected images. Note that the chief differences occur in the melt zones along the edges of the Greenland Ice Sheet, an area of great geophysical interest.

6.5   Selection of the Number of SIR Iterations

Figure 24 shows the difference between the SAR reference image and the SIR image versus the number of sir iterations. Some image examples are shown in Fig. 25. Note the initial decline in the root mean square (RMS) and standard deviation (std), followed by a slow rise. This is because each SIR iteration improves the signal error, but also enhances the noise. During the initial drop, the improvement in the signal component of the difference is larger than the rising noise level. As iteration conditions, the noise component begins to dominate. While the minimum error occurs at 4 or 5 iterations, subjectively, the image continues to improve for a while. Noting that the mean difference stabilizes by about 20
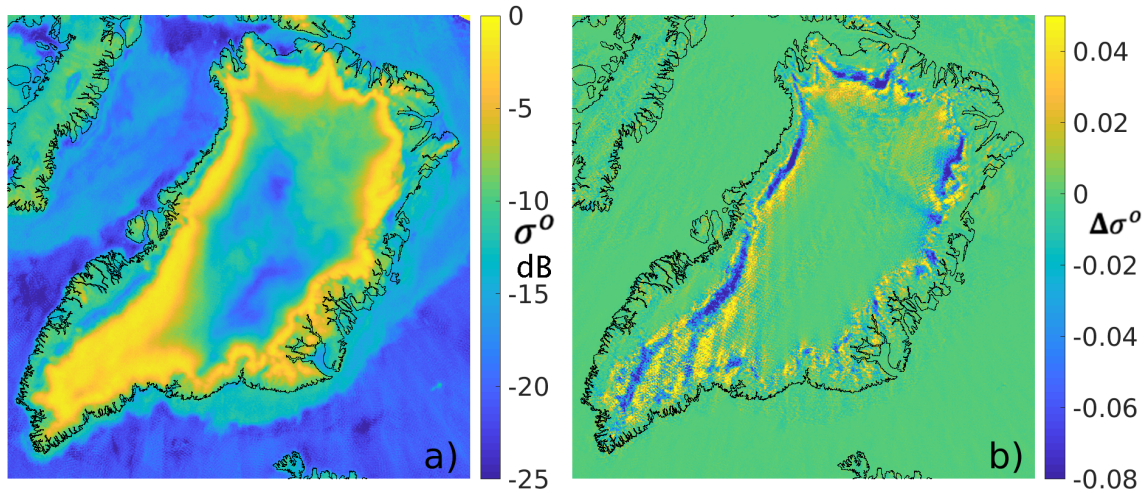
Figure 23: *(a) Evening, HH pol slice SIR σ^o in dB. On this scale the azimuth corrected and non-azimuth corrected appear similar. (b) Linear difference between the model-corrected σ^o and uncorrected SIR images.*

iterations, this value is selected for processing the full data set.
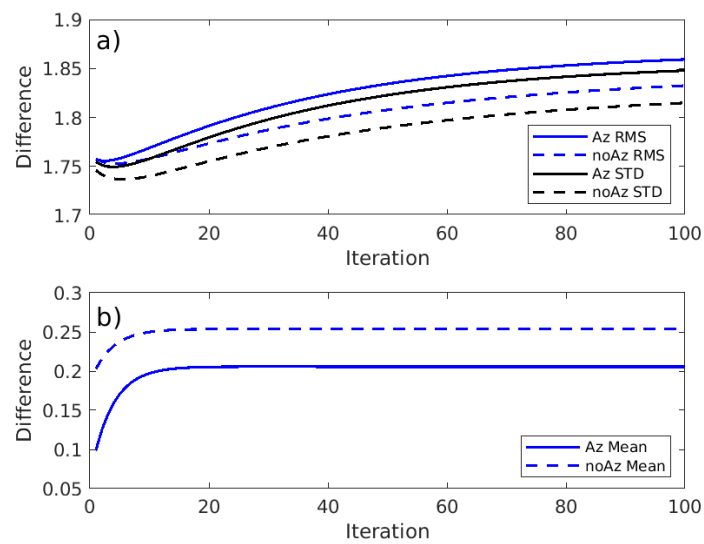
Figure 24: *Plot of RMS difference between slice SIR σ^o and SAR GRD σ^o values for Greenland for M and MI124 models. (a) Difference RMS and STD, (b) Mean difference.*
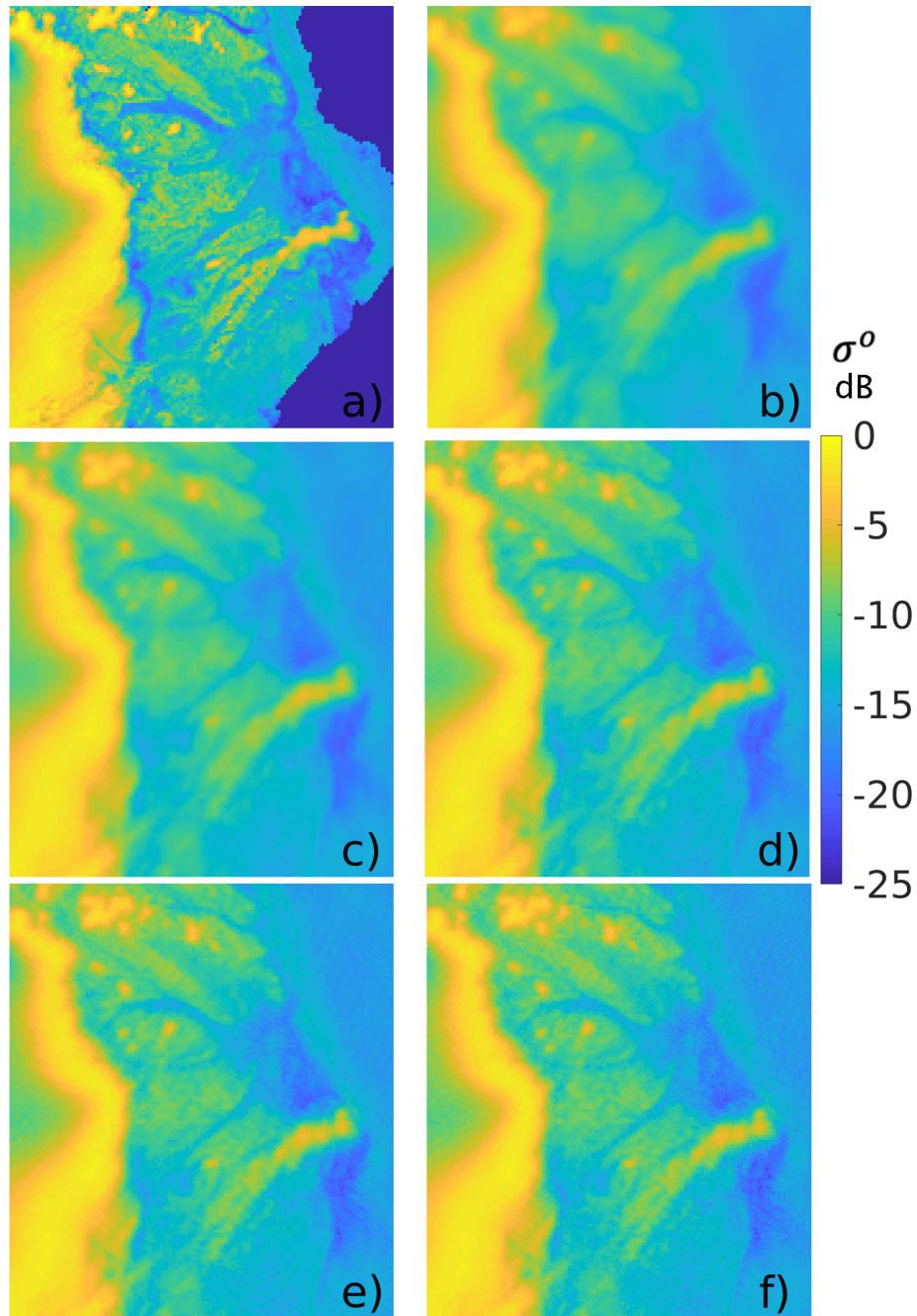
Figure 25: *Zoom-in σ^o comparison images in dB. (a) SAR GRD, (b) AVE (first SIR iteration), (c) 5 SIR iterations, (d) 20 SIR iterations, (e) 50 SIR iterations, (f) 100 SIR iterations.*

6.6   Data Volume

SMAP radar data extends from day 103 to day 186, 2015. During the initial 8 days, default SAR data selection tables were used by the radar. These provided small, even-spaced patches of SAR data. Later the radar control tables were updated to collect data over most land regions, except Antarctica.

SAR-SIR-SMAP images are made from all available radar data not flagged as "bad". No calibration corrections were applied to the data. Table 5 summarizes available SAR-SIR-SMAP radar image products, which are all in CETB-standard EASE-2 Grid projections. In this table, "days" refers to the length of time used for image formation. Imaging periods overlap, with a new image started each day. Individual file sizes vary due to internal file compression for each image type. See Section 4.5 for access details.

7 Acknowledgements

8 References

References

Ashcraft, I. S. and D. G. Long. 2006. Relating microwave backscatter azimuth modulation to surface properties of the Greenland ice sheet. *Journal of Glaciology 52*(177), 257–266. doi:`10.3189/172756506781828764`.

Brodzik, M. J., B. Billingsley, T. Haran, B. Raup, and M. H. Savoie. 2012. EASE-Grid 2.0: Incremental but significant improvements for Earth-gridded data sets. *International Society for Photogrammetry and Remote Sensing 1*, 32–45. doi:`10.3390/ijgi101003`.

Brodzik, M. J., B. Billingsley, T. Haran, B. Raup, and M. H. Savoie. 2014. Correction: Brodzik, M.J., *et al.* EASE-Grid 2.0: Incremental but Significant Improvements for Earth-Gridded Data Sets, *ISPRS Int. J. Geo-Inf.* 2012, 1, 32–45. *ISPRS Int. J. Geo-Inf. 3*, 1154–1156. doi:`10.3390/ijgi3031154`.

Brodzik, M. J. and K. Knowles. 2011. EASE-Grid 2.0 Land-Ocean-Coastline-Ice Masks Derived from Boston University MODIS/Terra Land Cover Data. NASA National Snow and Ice Data Center DAAC, Boulder, CO USA. Digital Media, `http://nsidc.org/data/nsidc-0610`, doi:`https://doi.org/10.5067/XR8523MC24TB`.

Brodzik, M. J., D. G. Long, M. A. Hardman, A. Paget, and R. L. Armstrong. 2016, updated 2021. MEaSUREs Calibrated Enhanced-Resolution Passive Microwave Daily EASE-Grid 2.0 Brightness Temperature ESDR, Version 1. National Snow and Ice Data Center, Boulder, CO USA. Digital Media, `http://nsidc.org/data/nsidc-0630`, doi:`https://doi.org/10.5067/MEASURES/CRYOSPHERE/NSIDC-0630.001`.

Brodzik, M. J., J. M. Ramage, M. A. Hardman, D. G. Long, and R. L. Armstrong. 2018. Improving melt onset detection in mountainous regions from the new, enhanced-resolution passive microwave climate record. Poster presentation at EGU General Assembly, CR 2.1:10690, Vienna, Austria, 9–13 April.

Early, D. S. and D. G. Long. 2001. Image reconstruction and enhanced resolution imaging from irregular samples. *IEEE Transactions on Geoscience and Remote Sensing 39*(2), 291–302. doi:`10.1109/36.905237`.

Entekhabi, D., E. G. Njoku, P. E. O'Neill, K. H. Kellogg, W. T. Crow, W. N. Edelstein, J. K. Entin, S. D. Goodman, T. J. Jackson, J. Johnson, J. Kimball, J. R. Piepmeier, R. D. Koster, N. Martin, K. C. McDonald, M. Moghaddam, S. Moran, R. Reichle, J. C. Shi, M. W. Spencer, S. W. Thurman, L. Tsang, and J. Van Zyl. 2010. The Soil Moisture Active Passive (SMAP) Mission. *Proceedings of the IEEE 98*(5), 704–716.

Entekhabi, D., S. Yueh, P. E. O'Neill, K. H. Kellog, A. Allen, R. Bindlish, et al.. 2014. *SMAP Handbook–Soil Moisture Active Passive: Mapping Soil Moisture and Freeze/Thaw from Space*. Number JPL CL#14-2285. Pasadena, CA, USA: Jet Propulsion Laboratory. `https://smap.jpl.nasa.gov/files/smap2/SMAP_Handbook_FINAL_1_JULY_2014_Web.pdf`.

Lindsley, R. and D. Long. 2016. ASCAT and QuikSCAT azimuth modulation of backscatter over East Antarctica. *IEEE Geoscience and Remote Sensing Letters, 13*(8), 1134–1138. doi:`10.1109/LGRS.2016.2572101`.

Long, D.. 2017. Comparison of SeaWinds backscatter imaging algorithms. *IEEE J. Sel. Topics in Applied Earth Observations 10*(3), 2214–2231. doi:`10.1109/JSTARS.2016.2626966`.

Long, D. and M. Brodzik. 2016a. Optimum image formation for spaceborne microwave radiometer products. *IEEE Trans. Geosci. Remote Sensing 54*(5), 2763–2779. doi:`10.1109/TGARS.2015.2505677`.

Long, D. and D. Daum. 1998. Spatial resolution enhancement of SSM/I data. *IEEE Trans. Geosci. Remote Sensing 36*(2), 407–417.

Long, D. and M. Drinkwater. 2000. Azimuth variation in microwave scatterometer and radiometer data over Antarctica. *IEEE Transactions on Geoscience and Remote Sensing 38*(4), 1857–1870. doi:`10.1109/36.851769`.

Long, D. and R. Franz. 2016. Band-limited signal reconstruction from irregular samples with variable apertures. *IEEE Transactions on Geoscience and Remote Sensing 54*(4), 2424–2436. doi:`10.1109/TGRS.2015.2501366`.

Long, D., P. Hardin, and P. Whiting. 1993. Resolution enhancement of spaceborne scatterometer data. *IEEE Trans. Geosci. Remote Sensing 31*(3), 700–715. doi:`10.1109/36.225536`.

Long, D. G. and M. J. Brodzik. 2016b, May. Optimum Image Formation for Spaceborne Microwave Radiometer Products. *IEEE Transactions on Geoscience and Remote Sensing 54*(5), 2763–2779. doi:`10.1109/TGRS.2015.2505677`.

Long, D. G., M. J. Brodzik, and M. A. Hardman. 2019. Enhanced–Resolution SMAP Brightness Temperature Image Products. *IEEE Transactions on Geoscience and Remote Sensing 57*(7), 4151–4163. doi:`10.1109/TGRS.2018.2889427`.

Meissner, T., L. R. and F. Wentz. 2017. Capability of the SMAP mission to measure ocean surface winds in storms. *Bulletin of the American Meteorological Society 98*(8), 1660–1677. doi:`10.1175/BAMS-D-16-0052.1`.

Miller, J. Z., D. Long, M. Hardman, and M. J. Brodzik. in prep, 2022. SMAP enhanced resolution radar scatterometer and synthetic aperture radar image products. *Earth System Science Data*.

Piepmeier, J, P. Mohammed, G. DeAmici, E. Kim, J. Peng, and C. Ruf. 2016. Algorithm Theortical Basis Document SMAP L1B Radiometer Brightness Temperature Data Product: L1B_TB (Includes L1A and L1B) Rev. B. NASA Goddard Space Flight Center, USA. Digital Media, `https://ntrs.nasa.gov/archive/nasa/casi.ntrs.nasa.gov/20160003317.pdf`.

Piepmeier, J. R., P. Focardi, K. A. Horgan, J. Knuble, N. Ehsan, J. Lucey, C. Brambora, P. R. Brown, P. J. Hoffman, R. T. French, R. L. Mikhaylov, E. Kwack, E. M. Slimko, D. E. Dawson, D. Hudson, J. Peng, P. N. Mohammed, G. De Amici, A. P. Freedman, J. Medeiros, F. Sacks, R. Estep, M. W. Spencer, C. W. Chen, K. B. Wheeler, W. N. Edelstein, P. E. O'Neill, and E. G. Njoku. 2017. SMAP L–Band Microwave Radiometer: Instrument Design and First Year on Orbit. *IEEE Transactions on Geoscience and Remote Sensing 55*(4), 1954–1966.

Pitas, I. and A. Venetsanopoulos. 1986. Nonlinear mean filters in image processing. *IEEE Transactions on Acoustics, Speech, and Signal Processing 34*(3), 573–584. doi:`10.1109/TASSP.1986.1164857`.

Stephen, H. and D. G. Long. 2007. Spatial and temporal behavior of microwave backscatter directional modulation over the Saharan ergs. *IEEE Transactions on Geoscience and Remote Sensing 45*(5), 1164–1173. doi:`10.1109/TGRS.2007.892584`.

West, R.. 2014. Soil Moisture Active Passive (SMAP) L1B_S0, L1C_S0, Algorithm Theoretical Basis Document (ATBD). Jet Propulsion Laboratory, Pasadena, CA USA. `https://smap.jpl.nasa.gov/internal_resources/details/original/280_L1C_S0_RevA_web.pdf`.

Wikipedia. visited 8 Oct. 2016. Geometric mean. Online, `http://en.wikipedia.org/wiki/Geometric_mean`.

Appendices

A *SAR-SIR-SMAP* Projections and Grids

Table 9: SAR-SIR-SMAP *25 km product EASE-Grid 2.0 projections and grid dimensions, produced for compatibility with CETB ESDR data products (Brodzik et al., 2021).*

Name	Projection	Resolution (km)	Cols	Rows	Latitude Extent	Longitude Extent
EASE2-T25km	Temperate and Tropical Cylindrical	25.025 260 00	1388	540	$\pm 67.057\,640\,6°$	$\pm 180°$
EASE2-T3.125km	Temperate and Tropical Cylindrical	3.128 157 50	11 104	4320	$\pm 67.057\,640\,6°$	$\pm 180°$
EASE2-N25km	Northern Lambert Azimuthal	25.0	720	720	$0°–90°$	$\pm 180°$
EASE2-N3.125km	Northern Lambert Azimuthal	3.125	5760	5760	$0°–90°$	$\pm 180°$
EASE2-S25km	Southern Lambert Azimuthal	25.0	720	720	$-90°–0°$	$\pm 180°$
EASE2-S3.125km	Southern Lambert Azimuthal	3.125	5760	5760	$-90°–0°$	$\pm 180°$

B *SAR-SIR-SMAP* Data Definition

B.1 File Requirements

Following Brodzik et al. (2021), *SAR-SIR-SMAP* product file requirements include:

- Files will conform to netCDF-CF 1.6 conventions for all but the requirement that puts the lat/lon arrays into the file; however, we will include CF-compliant coordinate variables with projected coordinate locations
- Files should pass CF-compliance-checking for all but the lat/lon arrays (we used JPL compliance-checker)
- Each file will contain 1 σ^o array variable, with associated ancillary variables, possibly different ancillary variables for each gridding technique. We may have a practical limit on the number of ancillary variables to include, limited by maximum file size
- Each file of the same type (GRD or rSIR) will contain the same file-level metadata for that type.
- We will follow the DRY (Don't Repeat Yourself) principle: Metadata will not be duplicated at multiple places in the same file
- DRY exception: Time values will be machine- and human-readable
- DRY exception: Some projection metadata may be in multiple forms (a proj4 string and/or a WKT string)
- Variable/attribute names will be CF-compliant whenever possible

The *SAR-SIR-SMAP* .nc files work with gdal utility, *gdal_translate,* to produce a geoTIFF version of each of the data variables <variable_name> in the file, (details in Brodzik et al. (2018)), for e.g.:

```
$ gdal_translate -of GTiff -b 1 \
NETCDF:''cetb.nc'':<variable_name> variable_name.tif
```

B.2 Filename Convention

SAR-SIR-SMAP data are distributed by the NSIDC DAAC (http://nsidc.org/data/nsidc-0774). Filenames are:
<product_id>-<grid_name>-<platform_sensor>-<yyyyddd-yyyyddd>
  -<channel_id>-<pass>-<algorithm>-<input_source>-<version>.nc
where parts of the filename are described in Table 10.

B.3 File Content, v1.0

The following is a sample NetCDF *ncdump –h* utility output for a *SAR-SIR-SMAP* v1.0 3.125 km slice SIR file. File-level metadata and processing details vary depending on projection, spa-

Table 10: SAR-SIR-SMAP *file naming convention*

Part	Description	Values
<product_id>	NSIDC unique data product id	NSIDC-0774
<grid_name>	EASE-Grid 2.0 grid id	See Table 9
<platform>	Satellite platform	SMAP
<sensor>	Sensor name	Radar
<yyyyddd-yyyyddd >	Date range	4-digit year and 3-digit day-of-year
<channel_id>	Channel (frequency in GHz and polarization)	1.2 followed by polarization, one of: • HH = horizontal-horizontal • VV = vertical-vertical • HV = horizontal-vertical • VH = vertical-horizontal • XX = cross-pol (averaged VH and HV)
<pass>	Pass direction (T grids) or ltod (N or S grids)	one of: • A = Ascending • D = Descending • M = Morning • E = Evening
<algorithm>	Reconstruction algorithm	one of GRD, AVE, or SIR
<version>	Version number	production version number

tial resolution and processing details (method, input file list, etc.). Only 3.125 km slice SIR files include the Sigma0_slope and Az_mod* variables, but other variables (time, x, y, crs, Sigma0, Sigma0_num_samples, angle_of_incidence, Sigma0_time) are common to all file types

```
netcdf NSIDC-0774-EASE2_S3.125km-SMAP_Radar_Slice-2015151_2015158-1.2HH-E-SIR-v1.0 {
dimensions:
time = UNLIMITED ; // (1 currently)
y = 5760 ;
x = 5760 ;
variables:
double time(time) ;
time:standard_name = "time" ;
time:coverage_content_type = "coordinate" ;
```

```
time:long_name = "ANSI date" ;
time:units = "days since 1972-01-01 00:00:00" ;
time:calendar = "gregorian" ;
time:axis = "T" ;
time:valid_range = 0., 1.79769313486232e+308 ;
double y(y) ;
y:standard_name = "projection_y_coordinate" ;
y:coverage_content_type = "coordinate" ;
y:long_name = "y" ;
y:units = "meters" ;
y:axis = "Y" ;
y:valid_range = -9000000., 9000000. ;
double x(x) ;
x:standard_name = "projection_x_coordinate" ;
x:coverage_content_type = "coordinate" ;
x:long_name = "x" ;
x:units = "meters" ;
x:axis = "X" ;
x:valid_range = -9000000., 9000000. ;
char crs ;
crs:grid_mapping_name = "lambert_azimuthal_equal_area" ;
crs:longitude_of_projection_origin = 0. ;
crs:latitude_of_projection_origin = -90. ;
crs:false_easting = 0. ;
crs:false_northing = 0. ;
crs:semi_major_axis = 6378137. ;
crs:inverse_flattening = 298.257223563 ;
crs:proj4text = "+proj=laea +lat_0=-90 +lon_0=0 +x_0=0 +y_0=0 +ellps=WGS84 +datum=WGS84 +units=m" ;
crs:srid = "urn:ogc:def:crs:EPSG::6932" ;
crs:coverage_content_type = "auxiliaryInformation" ;
crs:references = "[\"EASE-Grid 2.0 documentation: http://nsidc.org/data/ease/ease_grid2.html\", \"Brodzi
crs:crs_wkt = "PROJCRS[\"WGS 84 / NSIDC EASE-Grid 2.0 South\", BASEGEODCRS[\"WGS 84\", DATUM[\"World Geo
crs:long_name = "EASE2_S3.125km" ;
short Sigma0(time, y, x) ;
Sigma0:long_name = "SIR Sigma0" ;
Sigma0:units = "1" ;
Sigma0:comments = "unitless, in dB=10log_10" ;
Sigma0:_FillValue = -32768s ;
Sigma0:valid_range = 0s, 32767s ;
Sigma0:packing_convention = "netCDF" ;
Sigma0:packing_convention_description = "unpacked = scale_factor*packed + add_offset" ;
Sigma0:scale_factor = 0.002f ;
Sigma0:add_offset = -55.f ;
Sigma0:grid_mapping = "crs" ;
Sigma0:coverage_content_type = "image" ;
Sigma0:sir_number_of_iterations = 20 ;
Sigma0:median_filter = 0 ;
Sigma0:temporal_division = "Evening" ;
```

```
Sigma0:temporal_division_local_start_time = 12.f ;
Sigma0:temporal_division_local_end_time = 24.f ;
Sigma0:frequency_and_polarization = "1.4HH" ;
short Sigma0_num_samples(time, y, x) ;
Sigma0_num_samples:long_name = "Number of Measurements" ;
Sigma0_num_samples:units = "count" ;
Sigma0_num_samples:_FillValue = 0s ;
Sigma0_num_samples:valid_range = 1s, 32767s ;
Sigma0_num_samples:grid_mapping = "crs" ;
Sigma0_num_samples:coverage_content_type = "auxiliaryInformation" ;
short angle_of_incidence(time, y, x) ;
angle_of_incidence:standard_name = "angle_of_incidence" ;
angle_of_incidence:long_name = "Incidence Angle" ;
angle_of_incidence:units = "degree" ;
angle_of_incidence:_FillValue = -1s ;
angle_of_incidence:valid_range = 0s, 9000s ;
angle_of_incidence:packing_convention = "netCDF" ;
angle_of_incidence:packing_convention_description = "unpacked = scale_factor*packed + add_offset" ;
angle_of_incidence:scale_factor = 0.01f ;
angle_of_incidence:add_offset = 0.f ;
angle_of_incidence:grid_mapping = "crs" ;
angle_of_incidence:coverage_content_type = "auxiliaryInformation" ;
short Sigma0_std_dev(time, y, x) ;
Sigma0_std_dev:long_name = "SIR Std Deviation" ;
Sigma0_std_dev:units = "1" ;
Sigma0_std_dev:comments = "unitless, in dB=10log_10" ;
Sigma0_std_dev:_FillValue = -32768s ;
Sigma0_std_dev:valid_range = -32766s, 32767s ;
Sigma0_std_dev:packing_convention = "netCDF" ;
Sigma0_std_dev:packing_convention_description = "unpacked = scale_factor*packed + add_offset" ;
Sigma0_std_dev:scale_factor = 0.002f ;
Sigma0_std_dev:add_offset = 0.f ;
Sigma0_std_dev:grid_mapping = "crs" ;
Sigma0_std_dev:coverage_content_type = "auxiliaryInformation" ;
short Sigma0_time(time, y, x) ;
Sigma0_time:standard_name = "time" ;
Sigma0_time:long_name = "SIR Time of Day" ;
Sigma0_time:units = "minutes since 2015-05-31 00:00:00" ;
Sigma0_time:_FillValue = -32768s ;
Sigma0_time:valid_range = -32767s, 32767s ;
Sigma0_time:grid_mapping = "crs" ;
Sigma0_time:coverage_content_type = "auxiliaryInformation" ;
Sigma0_time:calendar = "gregorian" ;
short Sigma0_slope(time, y, x) ;
Sigma0_slope:long_name = "derivative of Sigma0 wrt to incidence" ;
Sigma0_slope:units = "1" ;
Sigma0_slope:comments = "sigma0 per deg  model: sigma0_meas=Sigma0+Sigma0_slope*(incidence-40)+Az_mod1_a
Sigma0_slope:_FillValue = -32768s ;
```

```
Sigma0_slope:valid_range = -26000s, 26000s ;
Sigma0_slope:packing_convention = "netCDF" ;
Sigma0_slope:packing_convention_description = "unpacked = scale_factor*packed + add_offset" ;
Sigma0_slope:scale_factor = 0.001f ;
Sigma0_slope:add_offset = 0.f ;
Sigma0_slope:grid_mapping = "crs" ;
Sigma0_slope:coverage_content_type = "auxiliaryInformation" ;
short Az_mod1_amp(time, y, x) ;
Az_mod1_amp:long_name = "Amplitude of 1st order azimuth modulation" ;
Az_mod1_amp:units = "1" ;
Az_mod1_amp:comments = "in dB=10log_10  model: sigma0_meas=Sigma0+Sigma0_slope*(incidence-40)+Az_mod1_am
Az_mod1_amp:_FillValue = -32000s ;
Az_mod1_amp:valid_range = -30000s, 30000s ;
Az_mod1_amp:packing_convention = "netCDF" ;
Az_mod1_amp:packing_convention_description = "unpacked = scale_factor*packed + add_offset" ;
Az_mod1_amp:scale_factor = 0.0005f ;
Az_mod1_amp:add_offset = -1.f ;
Az_mod1_amp:grid_mapping = "crs" ;
Az_mod1_amp:coverage_content_type = "auxiliaryInformation" ;
short Az_mod1_ang(time, y, x) ;
Az_mod1_ang:long_name = "Angle of 1st order azimuth modulation" ;
Az_mod1_ang:units = "degree" ;
Az_mod1_ang:comments = "in deg  model: sigma0_meas=Sigma0+Sigma0_slope*(incidence-40)+Az_mod1_amp*cos(4p
Az_mod1_ang:_FillValue = -18100s ;
Az_mod1_ang:valid_range = -18000s, 18000s ;
Az_mod1_ang:packing_convention = "netCDF" ;
Az_mod1_ang:packing_convention_description = "unpacked = scale_factor*packed + add_offset" ;
Az_mod1_ang:scale_factor = 0.05f ;
Az_mod1_ang:add_offset = 180.f ;
Az_mod1_ang:grid_mapping = "crs" ;
Az_mod1_ang:coverage_content_type = "auxiliaryInformation" ;
short Az_mod2_amp(time, y, x) ;
Az_mod2_amp:long_name = "Amplitude of 2nd order azimuth modulation" ;
Az_mod2_amp:units = "1" ;
Az_mod2_amp:comments = "in dB=10log_10  model: sigma0_meas=Sigma0+Sigma0_slope*(incidence-40)+Az_mod1_am
Az_mod2_amp:_FillValue = -32000s ;
Az_mod2_amp:valid_range = -30000s, 30000s ;
Az_mod2_amp:packing_convention = "netCDF" ;
Az_mod2_amp:packing_convention_description = "unpacked = scale_factor*packed + add_offset" ;
Az_mod2_amp:scale_factor = 0.0005f ;
Az_mod2_amp:add_offset = -1.f ;
Az_mod2_amp:grid_mapping = "crs" ;
Az_mod2_amp:coverage_content_type = "auxiliaryInformation" ;
short Az_mod2_ang(time, y, x) ;
Az_mod2_ang:long_name = "Angle of 2nd order azimuth modulation" ;
Az_mod2_ang:units = "degree" ;
Az_mod2_ang:comments = "in deg  model: sigma0_meas=Sigma0+Sigma0_slope*(incidence-40)+Az_mod1_amp*cos(4p
Az_mod2_ang:_FillValue = -18100s ;
```

```
Az_mod2_ang:valid_range = -18000s, 18000s ;
Az_mod2_ang:packing_convention = "netCDF" ;
Az_mod2_ang:packing_convention_description = "unpacked = scale_factor*packed + add_offset" ;
Az_mod2_ang:scale_factor = 0.05f ;
Az_mod2_ang:add_offset = 180.f ;
Az_mod2_ang:grid_mapping = "crs" ;
Az_mod2_ang:coverage_content_type = "auxiliaryInformation" ;


// global attributes:
:_NCProperties = "version=2,netcdf=4.9.0,hdf5=1.8.16" ;
:references = "West, R. 2014. Soil Moisture Active Passive Mission (SMAP) L1B_S0, L1C_S0, Algorithm The
:title = "SMAP Radar SAR and SIR-Enhanced Twice-Daily EASE-Grid 2.0 Radar Backscatter" ;
:id = "doi:10.5067/SCKWZSWQ7HPL" ;
:summary = "Averaged SAR and SIR-enhanced-resolution SMAP L-band radar backscatter on twice-daily EASE-
:project = "Scatterometer Climate Record Pathfinder" ;
:contributor_name = "David G. Long (NASA Scatterometer Climate Record Pathfinder), Julie Z. Miller (NAS
:contributor_role = "Principal Investigator, Co-Investigator" ;
:citation = "Long, D. G., and J. Z. Miller. 2022.\nSMAP Radar SAR and SIR-Enhanced Twice-Daily EASE-Gri
:license = "These data are freely, openly, and fully available to use without\nrestrictions, provided t
:Conventions = "CF-1.6, ACDD-1.3" ;
:product_version = "v1.0" ;
:history = "meas_meta_sir2bradar_CETB4" ;
:comment = "Epoch date for data in this file: 2015-05-31 00:00:00Z" ;
:source = "https://nsidc.org/data/SPL1BS0/versions/1 : See input_fileN list and number_of_input_files a
:metadata_link = "http://nsidc.org/data/NSIDC-0774.html" ;
:institution = "NASA National Snow and Ice Data Center Distributed Active Archive Center\nNational Snow
:publisher_name = "NASA National Snow and Ice Data Center Distributed Active Archive Center" ;
:publisher_type = "institution" ;
:publisher_url = "http://nsidc.org" ;
:publisher_email = "nsidc@nsidc.org" ;
:program = "NASA Terrestial Hydrology Program SMAP Science Team and NASA Cryospheric Sciences Research" 
:standard_name_vocabulary = "CF Standard Name Table (v78, 21 September 2021)" ;
:cdm_data_type = "Grid" ;
:keywords = "EARTH SCIENCE > SPECTRAL/ENGINEERING > MICROWAVE > RADAR BACKSCATTER" ;
:keywords_vocabulary = "NASA Global Change Master Directory (GCMD) Earth Science Keywords, Version 12.3
:platform = "SMAP > Soil Moisture Active and Passive Observatory" ;
:platform_vocabulary = "NASA Global Change Master Directory (GCMD) Earth Science Keywords, Version 12.3
:instrument = "SMAP L-BAND RADAR > SMAP L-Band Radar Scatterometer mode (slices)" ;
:instrument_vocabulary = "NASA Global Change Master Directory (GCMD) Earth Science Keywords, Version 12
:time_coverage_resolution = "P1d" ;
:geospatial_lat_min = -90. ;
:geospatial_lat_max = 0. ;
:geospatial_lon_min = -180. ;
:geospatial_lon_max = 180. ;
:geospatial_lat_units = "degree_north" ;
:geospatial_lon_units = "degree_east" ;
:geospatial_x_units = "meters" ;
:geospatial_y_units = "meters" ;
```

```
:naming_authority = "org.doi.dx" ;
:input_data_quality_filtering = "Only uses highest-quality input data." ;
:acknowledgement = "This data set was created with funding from NASA 2016 ROSES (Research Opportunities
:processing_level = "Level 3" ;
:creator_name = "David Long" ;
:creator_type = "person" ;
:creator_email = "long@ee.byu.edu" ;
:creator_url = "http://www.scp.byu.edu" ;
:creator_institution = "Microwave Earth Remote Sensing Laboratory\nElectrical and Computer Engineering I
:software_version_id = "1.0.0" ;
:geospatial_x_resolution = "3125.00 meters" ;
:geospatial_y_resolution = "3125.00 meters" ;
:number_of_input_files = 244 ;
:input_file1 = "SMAP_L1B_S0_LORES_01747_A_20150530T235325_R13080_001.h5" ;
:input_file2 = "SMAP_L1B_S0_LORES_01747_A_20150530T235325_R13080_001.h5" ;
:input_file3 = "SMAP_L1B_S0_LORES_01747_D_20150531T004236_R13080_001.h5" ;
:input_file4 = "SMAP_L1B_S0_LORES_01748_A_20150531T013151_R13080_001.h5" ;
:input_file5 = "SMAP_L1B_S0_LORES_01748_D_20150531T022106_R13080_001.h5" ;
:input_file6 = "SMAP_L1B_S0_LORES_01749_A_20150531T031021_R13080_001.h5" ;
:input_file7 = "SMAP_L1B_S0_LORES_01749_D_20150531T035931_R13080_001.h5" ;
:input_file8 = "SMAP_L1B_S0_LORES_01750_A_20150531T044846_R13080_001.h5" ;
:input_file9 = "SMAP_L1B_S0_LORES_01750_D_20150531T053801_R13080_001.h5" ;
:input_file10 = "SMAP_L1B_S0_LORES_01751_A_20150531T062716_R13080_001.h5" ;
:input_file11 = "SMAP_L1B_S0_LORES_01751_D_20150531T071627_R13080_001.h5" ;
:input_file12 = "SMAP_L1B_S0_LORES_01752_A_20150531T080541_R13080_001.h5" ;
:input_file13 = "SMAP_L1B_S0_LORES_01752_D_20150531T085456_R13080_001.h5" ;
:input_file14 = "SMAP_L1B_S0_LORES_01753_A_20150531T094411_R13080_001.h5" ;
:input_file15 = "SMAP_L1B_S0_LORES_01753_D_20150531T103322_R13080_001.h5" ;
:input_file16 = "SMAP_L1B_S0_LORES_01754_A_20150531T112237_R13080_001.h5" ;
:input_file17 = "SMAP_L1B_S0_LORES_01754_D_20150531T121151_R13080_001.h5" ;
:input_file18 = "SMAP_L1B_S0_LORES_01755_A_20150531T130106_R13080_001.h5" ;
:input_file19 = "SMAP_L1B_S0_LORES_01755_D_20150531T135021_R13080_001.h5" ;
:input_file20 = "SMAP_L1B_S0_LORES_01756_A_20150531T143932_R13080_001.h5" ;
:input_file21 = "SMAP_L1B_S0_LORES_01756_D_20150531T152847_R13080_001.h5" ;
:input_file22 = "SMAP_L1B_S0_LORES_01757_A_20150531T161802_R13080_001.h5" ;
:input_file23 = "SMAP_L1B_S0_LORES_01757_D_20150531T170716_R13080_001.h5" ;
:input_file24 = "SMAP_L1B_S0_LORES_01758_A_20150531T175627_R13080_001.h5" ;
:input_file25 = "SMAP_L1B_S0_LORES_01758_D_20150531T184542_R13080_001.h5" ;
:input_file26 = "SMAP_L1B_S0_LORES_01759_A_20150531T193457_R13080_001.h5" ;
:input_file27 = "SMAP_L1B_S0_LORES_01759_D_20150531T202412_R13080_001.h5" ;
:input_file28 = "SMAP_L1B_S0_LORES_01760_A_20150531T211322_R13080_001.h5" ;
:input_file29 = "SMAP_L1B_S0_LORES_01760_D_20150531T220237_R13080_001.h5" ;
:input_file30 = "SMAP_L1B_S0_LORES_01761_A_20150531T225152_R13080_001.h5" ;
:input_file31 = "SMAP_L1B_S0_LORES_01761_D_20150531T234107_R13080_001.h5" ;
:input_file32 = "SMAP_L1B_S0_LORES_01761_D_20150531T234107_R13080_001.h5" ;
:input_file33 = "SMAP_L1B_S0_LORES_01762_A_20150601T003018_R13080_001.h5" ;
:input_file34 = "SMAP_L1B_S0_LORES_01762_D_20150601T011932_R13080_001.h5" ;
:input_file35 = "SMAP_L1B_S0_LORES_01763_A_20150601T020847_R13080_001.h5" ;
```

```
:input_file36 = "SMAP_L1B_S0_LORES_01763_D_20150601T025802_R13080_001.h5" ;
:input_file37 = "SMAP_L1B_S0_LORES_01764_A_20150601T034713_R13080_001.h5" ;
:input_file38 = "SMAP_L1B_S0_LORES_01764_D_20150601T043628_R13080_001.h5" ;
:input_file39 = "SMAP_L1B_S0_LORES_01765_A_20150601T052542_R13080_001.h5" ;
:input_file40 = "SMAP_L1B_S0_LORES_01765_D_20150601T061457_R13080_001.h5" ;
:input_file41 = "SMAP_L1B_S0_LORES_01766_A_20150601T070408_R13080_001.h5" ;
:input_file42 = "SMAP_L1B_S0_LORES_01766_D_20150601T075323_R13080_001.h5" ;
:input_file43 = "SMAP_L1B_S0_LORES_01767_A_20150601T084238_R13080_001.h5" ;
:input_file44 = "SMAP_L1B_S0_LORES_01767_D_20150601T093152_R13080_001.h5" ;
:input_file45 = "SMAP_L1B_S0_LORES_01768_A_20150601T102103_R13080_001.h5" ;
:input_file46 = "SMAP_L1B_S0_LORES_01768_D_20150601T111018_R13080_001.h5" ;
:input_file47 = "SMAP_L1B_S0_LORES_01769_A_20150601T115933_R13080_001.h5" ;
:input_file48 = "SMAP_L1B_S0_LORES_01769_D_20150601T124848_R13080_001.h5" ;
:input_file49 = "SMAP_L1B_S0_LORES_01770_A_20150601T133803_R13080_001.h5" ;
:input_file50 = "SMAP_L1B_S0_LORES_01770_D_20150601T142713_R13080_001.h5" ;
:input_file51 = "SMAP_L1B_S0_LORES_01771_A_20150601T151628_R13080_001.h5" ;
:input_file52 = "SMAP_L1B_S0_LORES_01771_D_20150601T160543_R13080_001.h5" ;
:input_file53 = "SMAP_L1B_S0_LORES_01772_A_20150601T165458_R13080_001.h5" ;
:input_file54 = "SMAP_L1B_S0_LORES_01772_D_20150601T174408_R13080_001.h5" ;
:input_file55 = "SMAP_L1B_S0_LORES_01773_A_20150601T183323_R13080_001.h5" ;
:input_file56 = "SMAP_L1B_S0_LORES_01773_D_20150601T192238_R13080_001.h5" ;
:input_file57 = "SMAP_L1B_S0_LORES_01774_A_20150601T201153_R13080_001.h5" ;
:input_file58 = "SMAP_L1B_S0_LORES_01774_D_20150601T210104_R13080_001.h5" ;
:input_file59 = "SMAP_L1B_S0_LORES_01775_A_20150601T215019_R13080_001.h5" ;
:input_file60 = "SMAP_L1B_S0_LORES_01775_D_20150601T223933_R13080_001.h5" ;
:input_file61 = "SMAP_L1B_S0_LORES_01776_A_20150601T232848_R13080_001.h5" ;
:input_file62 = "SMAP_L1B_S0_LORES_01776_A_20150601T232848_R13080_001.h5" ;
:input_file63 = "SMAP_L1B_S0_LORES_01776_D_20150602T001759_R13080_001.h5" ;
:input_file64 = "SMAP_L1B_S0_LORES_01777_A_20150602T010714_R13080_001.h5" ;
:input_file65 = "SMAP_L1B_S0_LORES_01777_D_20150602T015629_R13080_001.h5" ;
:input_file66 = "SMAP_L1B_S0_LORES_01778_A_20150602T024543_R13080_001.h5" ;
:input_file67 = "SMAP_L1B_S0_LORES_01778_D_20150602T033454_R13080_001.h5" ;
:input_file68 = "SMAP_L1B_S0_LORES_01779_A_20150602T042409_R13080_001.h5" ;
:input_file69 = "SMAP_L1B_S0_LORES_01779_D_20150602T051324_R13080_001.h5" ;
:input_file70 = "SMAP_L1B_S0_LORES_01780_A_20150602T060239_R13080_001.h5" ;
:input_file71 = "SMAP_L1B_S0_LORES_01780_D_20150602T065149_R13080_001.h5" ;
:input_file72 = "SMAP_L1B_S0_LORES_01781_A_20150602T074104_R13080_001.h5" ;
:input_file73 = "SMAP_L1B_S0_LORES_01781_D_20150602T083019_R13080_001.h5" ;
:input_file74 = "SMAP_L1B_S0_LORES_01782_A_20150602T091934_R13080_001.h5" ;
:input_file75 = "SMAP_L1B_S0_LORES_01782_D_20150602T100845_R13080_001.h5" ;
:input_file76 = "SMAP_L1B_S0_LORES_01783_A_20150602T105759_R13080_001.h5" ;
:input_file77 = "SMAP_L1B_S0_LORES_01783_D_20150602T114714_R13080_001.h5" ;
:input_file78 = "SMAP_L1B_S0_LORES_01784_A_20150602T123629_R13080_001.h5" ;
:input_file79 = "SMAP_L1B_S0_LORES_01784_D_20150602T132540_R13080_001.h5" ;
:input_file80 = "SMAP_L1B_S0_LORES_01785_A_20150602T141455_R13080_001.h5" ;
:input_file81 = "SMAP_L1B_S0_LORES_01785_D_20150602T150409_R13080_001.h5" ;
:input_file82 = "SMAP_L1B_S0_LORES_01786_A_20150602T155324_R13080_001.h5" ;
:input_file83 = "SMAP_L1B_S0_LORES_01786_D_20150602T164239_R13080_001.h5" ;
```

```
:input_file84 = "SMAP_L1B_S0_LORES_01787_A_20150602T173150_R13080_001.h5" ;
:input_file85 = "SMAP_L1B_S0_LORES_01787_D_20150602T182105_R13080_001.h5" ;
:input_file86 = "SMAP_L1B_S0_LORES_01788_A_20150602T191020_R13080_001.h5" ;
:input_file87 = "SMAP_L1B_S0_LORES_01788_D_20150602T195934_R13080_001.h5" ;
:input_file88 = "SMAP_L1B_S0_LORES_01789_A_20150602T204845_R13080_001.h5" ;
:input_file89 = "SMAP_L1B_S0_LORES_01789_D_20150602T213800_R13080_001.h5" ;
:input_file90 = "SMAP_L1B_S0_LORES_01790_A_20150602T222715_R13080_001.h5" ;
:input_file91 = "SMAP_L1B_S0_LORES_01790_D_20150602T231630_R13080_001.h5" ;
:input_file92 = "SMAP_L1B_S0_LORES_01790_D_20150602T231630_R13080_001.h5" ;
:input_file93 = "SMAP_L1B_S0_LORES_01791_A_20150603T000540_R13080_001.h5" ;
:input_file94 = "SMAP_L1B_S0_LORES_01791_D_20150603T005455_R13080_001.h5" ;
:input_file95 = "SMAP_L1B_S0_LORES_01792_A_20150603T014410_R13080_001.h5" ;
:input_file96 = "SMAP_L1B_S0_LORES_01792_D_20150603T023325_R13080_001.h5" ;
:input_file97 = "SMAP_L1B_S0_LORES_01793_A_20150603T032236_R13080_001.h5" ;
:input_file98 = "SMAP_L1B_S0_LORES_01793_D_20150603T045004_R13080_001.h5" ;
:input_file99 = "SMAP_L1B_S0_LORES_01794_A_20150603T050105_R13080_001.h5" ;
:input_file100 = "SMAP_L1B_S0_LORES_01794_D_20150603T055020_R13080_001.h5" ;
:input_file101 = "SMAP_L1B_S0_LORES_01795_A_20150603T063931_R13080_001.h5" ;
:input_file102 = "SMAP_L1B_S0_LORES_01795_D_20150603T072846_R13080_001.h5" ;
:input_file103 = "SMAP_L1B_S0_LORES_01796_A_20150603T081800_R13080_001.h5" ;
:input_file104 = "SMAP_L1B_S0_LORES_01796_D_20150603T090715_R13080_001.h5" ;
:input_file105 = "SMAP_L1B_S0_LORES_01797_A_20150603T095626_R13080_001.h5" ;
:input_file106 = "SMAP_L1B_S0_LORES_01797_D_20150603T104541_R13080_001.h5" ;
:input_file107 = "SMAP_L1B_S0_LORES_01798_A_20150603T113456_R13080_001.h5" ;
:input_file108 = "SMAP_L1B_S0_LORES_01798_D_20150603T122410_R13080_001.h5" ;
:input_file109 = "SMAP_L1B_S0_LORES_01799_A_20150603T131321_R13080_001.h5" ;
:input_file110 = "SMAP_L1B_S0_LORES_01799_D_20150603T140236_R13080_001.h5" ;
:input_file111 = "SMAP_L1B_S0_LORES_01800_A_20150603T145151_R13080_001.h5" ;
:input_file112 = "SMAP_L1B_S0_LORES_01800_D_20150603T154106_R13080_001.h5" ;
:input_file113 = "SMAP_L1B_S0_LORES_01801_A_20150603T163021_R13080_001.h5" ;
:input_file114 = "SMAP_L1B_S0_LORES_01801_D_20150603T171931_R13080_001.h5" ;
:input_file115 = "SMAP_L1B_S0_LORES_01802_A_20150603T180846_R13080_001.h5" ;
:input_file116 = "SMAP_L1B_S0_LORES_01802_D_20150603T185801_R13080_001.h5" ;
:input_file117 = "SMAP_L1B_S0_LORES_01803_A_20150603T194712_R13080_001.h5" ;
:input_file118 = "SMAP_L1B_S0_LORES_01803_D_20150603T203626_R13080_001.h5" ;
:input_file119 = "SMAP_L1B_S0_LORES_01804_A_20150603T212541_R13080_001.h5" ;
:input_file120 = "SMAP_L1B_S0_LORES_01804_D_20150603T221456_R13080_001.h5" ;
:input_file121 = "SMAP_L1B_S0_LORES_01805_A_20150603T230411_R13080_001.h5" ;
:input_file122 = "SMAP_L1B_S0_LORES_01805_D_20150603T235322_R13080_001.h5" ;
:input_file123 = "SMAP_L1B_S0_LORES_01805_D_20150603T235322_R13080_001.h5" ;
:input_file124 = "SMAP_L1B_S0_LORES_01806_A_20150604T004237_R13080_001.h5" ;
:input_file125 = "SMAP_L1B_S0_LORES_01806_D_20150604T013151_R13080_001.h5" ;
:input_file126 = "SMAP_L1B_S0_LORES_01807_A_20150604T022106_R13080_001.h5" ;
:input_file127 = "SMAP_L1B_S0_LORES_01807_D_20150604T031017_R13080_001.h5" ;
:input_file128 = "SMAP_L1B_S0_LORES_01808_A_20150604T035932_R13080_001.h5" ;
:input_file129 = "SMAP_L1B_S0_LORES_01808_D_20150604T044847_R13080_001.h5" ;
:input_file130 = "SMAP_L1B_S0_LORES_01809_A_20150604T053801_R13080_001.h5" ;
:input_file131 = "SMAP_L1B_S0_LORES_01809_D_20150604T062712_R13080_001.h5" ;
```

```
:input_file132 = "SMAP_L1B_S0_LORES_01810_A_20150604T071627_R13080_001.h5" ;
:input_file133 = "SMAP_L1B_S0_LORES_01810_D_20150604T080542_R13080_001.h5" ;
:input_file134 = "SMAP_L1B_S0_LORES_01811_A_20150604T085457_R13080_001.h5" ;
:input_file135 = "SMAP_L1B_S0_LORES_01811_D_20150604T094407_R13080_001.h5" ;
:input_file136 = "SMAP_L1B_S0_LORES_01812_A_20150604T103322_R13080_001.h5" ;
:input_file137 = "SMAP_L1B_S0_LORES_01812_D_20150604T112237_R13080_001.h5" ;
:input_file138 = "SMAP_L1B_S0_LORES_01813_A_20150604T121152_R13080_001.h5" ;
:input_file139 = "SMAP_L1B_S0_LORES_01813_D_20150604T130103_R13080_001.h5" ;
:input_file140 = "SMAP_L1B_S0_LORES_01814_A_20150604T135017_R13080_001.h5" ;
:input_file141 = "SMAP_L1B_S0_LORES_01814_D_20150604T143932_R13080_001.h5" ;
:input_file142 = "SMAP_L1B_S0_LORES_01815_A_20150604T152847_R13080_001.h5" ;
:input_file143 = "SMAP_L1B_S0_LORES_01815_D_20150604T161758_R13080_001.h5" ;
:input_file144 = "SMAP_L1B_S0_LORES_01816_A_20150604T170713_R13080_001.h5" ;
:input_file145 = "SMAP_L1B_S0_LORES_01816_D_20150604T175627_R13080_001.h5" ;
:input_file146 = "SMAP_L1B_S0_LORES_01817_A_20150604T184542_R13080_001.h5" ;
:input_file147 = "SMAP_L1B_S0_LORES_01817_D_20150604T193453_R13080_001.h5" ;
:input_file148 = "SMAP_L1B_S0_LORES_01818_A_20150604T202408_R13080_001.h5" ;
:input_file149 = "SMAP_L1B_S0_LORES_01818_D_20150604T211323_R13080_001.h5" ;
:input_file150 = "SMAP_L1B_S0_LORES_01819_A_20150604T220238_R13080_001.h5" ;
:input_file151 = "SMAP_L1B_S0_LORES_01819_D_20150604T225148_R13080_001.h5" ;
:input_file152 = "SMAP_L1B_S0_LORES_01820_A_20150604T234103_R13080_001.h5" ;
:input_file153 = "SMAP_L1B_S0_LORES_01820_A_20150604T234103_R13080_001.h5" ;
:input_file154 = "SMAP_L1B_S0_LORES_01820_D_20150605T003018_R13080_001.h5" ;
:input_file155 = "SMAP_L1B_S0_LORES_01821_A_20150605T011933_R13080_001.h5" ;
:input_file156 = "SMAP_L1B_S0_LORES_01821_D_20150605T020843_R13080_001.h5" ;
:input_file157 = "SMAP_L1B_S0_LORES_01822_A_20150605T025758_R13080_001.h5" ;
:input_file158 = "SMAP_L1B_S0_LORES_01822_D_20150605T034713_R13080_001.h5" ;
:input_file159 = "SMAP_L1B_S0_LORES_01823_A_20150605T043628_R13080_001.h5" ;
:input_file160 = "SMAP_L1B_S0_LORES_01823_D_20150605T052543_R13080_001.h5" ;
:input_file161 = "SMAP_L1B_S0_LORES_01824_A_20150605T061454_R13080_001.h5" ;
:input_file162 = "SMAP_L1B_S0_LORES_01824_D_20150605T070408_R13080_001.h5" ;
:input_file163 = "SMAP_L1B_S0_LORES_01825_A_20150605T075323_R13080_001.h5" ;
:input_file164 = "SMAP_L1B_S0_LORES_01825_D_20150605T084238_R13080_001.h5" ;
:input_file165 = "SMAP_L1B_S0_LORES_01826_A_20150605T093149_R13080_001.h5" ;
:input_file166 = "SMAP_L1B_S0_LORES_01826_D_20150605T102104_R13080_001.h5" ;
:input_file167 = "SMAP_L1B_S0_LORES_01827_A_20150605T111018_R13080_001.h5" ;
:input_file168 = "SMAP_L1B_S0_LORES_01827_D_20150605T115933_R13080_001.h5" ;
:input_file169 = "SMAP_L1B_S0_LORES_01828_A_20150605T124844_R13080_001.h5" ;
:input_file170 = "SMAP_L1B_S0_LORES_01828_D_20150605T133759_R13080_001.h5" ;
:input_file171 = "SMAP_L1B_S0_LORES_01829_A_20150605T142714_R13080_001.h5" ;
:input_file172 = "SMAP_L1B_S0_LORES_01829_D_20150605T151628_R13080_001.h5" ;
:input_file173 = "SMAP_L1B_S0_LORES_01830_A_20150605T160539_R13080_001.h5" ;
:input_file174 = "SMAP_L1B_S0_LORES_01830_D_20150605T165454_R13080_001.h5" ;
:input_file175 = "SMAP_L1B_S0_LORES_01831_A_20150605T174409_R13080_001.h5" ;
:input_file176 = "SMAP_L1B_S0_LORES_01831_D_20150605T183324_R13080_001.h5" ;
:input_file177 = "SMAP_L1B_S0_LORES_01832_A_20150605T192234_R13080_001.h5" ;
:input_file178 = "SMAP_L1B_S0_LORES_01832_D_20150605T201149_R13080_001.h5" ;
:input_file179 = "SMAP_L1B_S0_LORES_01833_A_20150605T210104_R13080_001.h5" ;
```

```
:input_file180 = "SMAP_L1B_S0_LORES_01833_D_20150605T215019_R13080_001.h5" ;
:input_file181 = "SMAP_L1B_S0_LORES_01834_A_20150605T223930_R13080_001.h5" ;
:input_file182 = "SMAP_L1B_S0_LORES_01834_D_20150605T232844_R13080_001.h5" ;
:input_file183 = "SMAP_L1B_S0_LORES_01834_D_20150605T232844_R13080_001.h5" ;
:input_file184 = "SMAP_L1B_S0_LORES_01835_A_20150606T001759_R13080_001.h5" ;
:input_file185 = "SMAP_L1B_S0_LORES_01835_D_20150606T010714_R13080_001.h5" ;
:input_file186 = "SMAP_L1B_S0_LORES_01836_A_20150606T015625_R13080_001.h5" ;
:input_file187 = "SMAP_L1B_S0_LORES_01836_D_20150606T024540_R13080_001.h5" ;
:input_file188 = "SMAP_L1B_S0_LORES_01837_A_20150606T033454_R13080_001.h5" ;
:input_file189 = "SMAP_L1B_S0_LORES_01837_D_20150606T042409_R13080_001.h5" ;
:input_file190 = "SMAP_L1B_S0_LORES_01838_A_20150606T051320_R13080_001.h5" ;
:input_file191 = "SMAP_L1B_S0_LORES_01838_D_20150606T060235_R13080_001.h5" ;
:input_file192 = "SMAP_L1B_S0_LORES_01839_A_20150606T065150_R13080_001.h5" ;
:input_file193 = "SMAP_L1B_S0_LORES_01839_D_20150606T074105_R13080_001.h5" ;
:input_file194 = "SMAP_L1B_S0_LORES_01840_A_20150606T083015_R13080_001.h5" ;
:input_file195 = "SMAP_L1B_S0_LORES_01840_D_20150606T091930_R13080_001.h5" ;
:input_file196 = "SMAP_L1B_S0_LORES_01841_A_20150606T100845_R13080_001.h5" ;
:input_file197 = "SMAP_L1B_S0_LORES_01841_D_20150606T105800_R13080_001.h5" ;
:input_file198 = "SMAP_L1B_S0_LORES_01842_A_20150606T114715_R13080_001.h5" ;
:input_file199 = "SMAP_L1B_S0_LORES_01842_D_20150606T123625_R13080_001.h5" ;
:input_file200 = "SMAP_L1B_S0_LORES_01843_A_20150606T132540_R13080_001.h5" ;
:input_file201 = "SMAP_L1B_S0_LORES_01843_D_20150606T141455_R13080_001.h5" ;
:input_file202 = "SMAP_L1B_S0_LORES_01844_A_20150606T150410_R13080_001.h5" ;
:input_file203 = "SMAP_L1B_S0_LORES_01844_D_20150606T155321_R13080_001.h5" ;
:input_file204 = "SMAP_L1B_S0_LORES_01845_A_20150606T164235_R13080_001.h5" ;
:input_file205 = "SMAP_L1B_S0_LORES_01845_D_20150606T173150_R13080_001.h5" ;
:input_file206 = "SMAP_L1B_S0_LORES_01846_A_20150606T182105_R13080_001.h5" ;
:input_file207 = "SMAP_L1B_S0_LORES_01846_D_20150606T191016_R13080_001.h5" ;
:input_file208 = "SMAP_L1B_S0_LORES_01847_A_20150606T195931_R13080_001.h5" ;
:input_file209 = "SMAP_L1B_S0_LORES_01847_D_20150606T204845_R13080_001.h5" ;
:input_file210 = "SMAP_L1B_S0_LORES_01848_A_20150606T213800_R13080_001.h5" ;
:input_file211 = "SMAP_L1B_S0_LORES_01848_D_20150606T222711_R13080_001.h5" ;
:input_file212 = "SMAP_L1B_S0_LORES_01849_A_20150606T231626_R13080_001.h5" ;
:input_file213 = "SMAP_L1B_S0_LORES_01849_A_20150606T231626_R13080_001.h5" ;
:input_file214 = "SMAP_L1B_S0_LORES_01849_D_20150607T000541_R13080_001.h5" ;
:input_file215 = "SMAP_L1B_S0_LORES_01850_A_20150607T005455_R13080_001.h5" ;
:input_file216 = "SMAP_L1B_S0_LORES_01850_D_20150607T014406_R13080_001.h5" ;
:input_file217 = "SMAP_L1B_S0_LORES_01851_A_20150607T023321_R13080_001.h5" ;
:input_file218 = "SMAP_L1B_S0_LORES_01851_D_20150607T032236_R13080_001.h5" ;
:input_file219 = "SMAP_L1B_S0_LORES_01852_A_20150607T041151_R13080_001.h5" ;
:input_file220 = "SMAP_L1B_S0_LORES_01852_D_20150607T050101_R13080_001.h5" ;
:input_file221 = "SMAP_L1B_S0_LORES_01853_A_20150607T055016_R13080_001.h5" ;
:input_file222 = "SMAP_L1B_S0_LORES_01854_A_20150607T072846_R13080_001.h5" ;
:input_file223 = "SMAP_L1B_S0_LORES_01854_D_20150607T081757_R13080_001.h5" ;
:input_file224 = "SMAP_L1B_S0_LORES_01855_A_20150607T090711_R13080_001.h5" ;
:input_file225 = "SMAP_L1B_S0_LORES_01855_D_20150607T095626_R13080_001.h5" ;
:input_file226 = "SMAP_L1B_S0_LORES_01856_A_20150607T104541_R13080_001.h5" ;
:input_file227 = "SMAP_L1B_S0_LORES_01856_D_20150607T113452_R13080_001.h5" ;
```

```
:input_file228 = "SMAP_L1B_S0_LORES_01857_A_20150607T122407_R13080_001.h5" ;
:input_file229 = "SMAP_L1B_S0_LORES_01857_D_20150607T131322_R13080_001.h5" ;
:input_file230 = "SMAP_L1B_S0_LORES_01858_A_20150607T140236_R13080_001.h5" ;
:input_file231 = "SMAP_L1B_S0_LORES_01858_D_20150607T145151_R13080_001.h5" ;
:input_file232 = "SMAP_L1B_S0_LORES_01859_A_20150607T154102_R13080_001.h5" ;
:input_file233 = "SMAP_L1B_S0_LORES_01859_D_20150607T163017_R13080_001.h5" ;
:input_file234 = "SMAP_L1B_S0_LORES_01860_A_20150607T171932_R13080_001.h5" ;
:input_file235 = "SMAP_L1B_S0_LORES_01860_D_20150607T180846_R13080_001.h5" ;
:input_file236 = "SMAP_L1B_S0_LORES_01861_A_20150607T185757_R13080_001.h5" ;
:input_file237 = "SMAP_L1B_S0_LORES_01861_D_20150607T194712_R13080_001.h5" ;
:input_file238 = "SMAP_L1B_S0_LORES_01862_A_20150607T203627_R13080_001.h5" ;
:input_file239 = "SMAP_L1B_S0_LORES_01862_D_20150607T212542_R13080_001.h5" ;
:input_file240 = "SMAP_L1B_S0_LORES_01863_A_20150607T221452_R13080_001.h5" ;
:input_file241 = "SMAP_L1B_S0_LORES_01863_D_20150607T230407_R13080_001.h5" ;
:input_file242 = "SMAP_L1B_S0_LORES_01864_A_20150607T235322_R13080_001.h5" ;
:input_file243 = "SMAP_L1B_S0_LORES_01864_A_20150607T235322_R13080_001.h5" ;
:input_file244 = "SMAP_L1B_S0_LORES_01865_A_20150608T013148_R13080_001.h5" ;
:date_created = "2022-08-22T09:30:00Z" ;
:date_modified = "2022-08-22T09:30:00Z" ;
:date_issued = "2022-08-22T09:30:00Z" ;
:date_metadata_modified = "2022-08-22T09:30:00Z" ;
:time_coverage_start = "2015-05-31T00:18:00Z" ;
:time_coverage_end = "2015-06-07T22:41:00Z" ;
:time_coverage_duration = "P7T22:23:00" ;
}
```